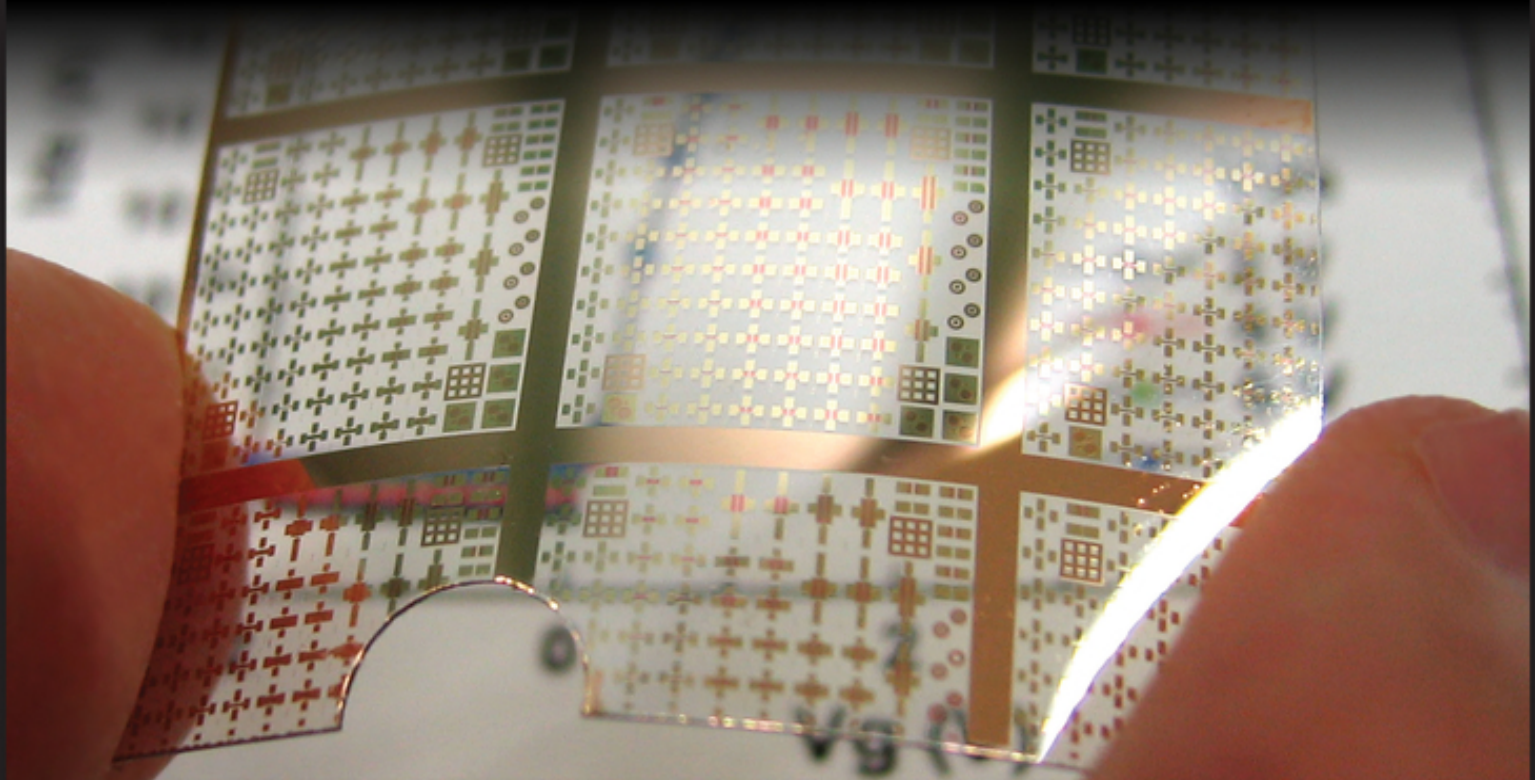


AMORPHOUS OXIDE SEMICONDUCTORS

IGZO and Related Materials
for Display and Memory

EDITORS

HIDEO HOSONO • HIDEYA KUMOMI



WILEY

SID

Series in **Display Technology**

Amorphous Oxide Semiconductors

Wiley–SID Series in Display Technology

Series Editor: Dr. Ian Sage

Advisory Board: Paul Drzaic, Ioannis (John) Kymissis, Ray Ma, Ian Underwood, Michael Wittek, and Qun (Frank) Yan

Flexible Flat Panel Displays, Second Edition

Darran R. Cairns, Dirk J. Broer, and Gregory P. Crawford

Liquid Crystal Displays – Addressing Schemes and Electro-Optical Effects, Third Edition

Ernst Lueder, Peter Knoll, and Seung Hee Lee

Amorphous Oxide Semiconductors: IGZO and Related Materials for Display and Memory

Hideo Hosono and Hideya Kumomi (Eds.)

Introduction to Flat Panel Displays, Second Edition

Jiun-Haw Lee, I-Chun Cheng, Hong Hua, and Shin-Tson Wu

Flat Panel Display Manufacturing

Jun Souk, Shinji Morozumi, Fang-Chen Luo, and Ion Bitu

Physics and Technology of Crystalline Oxide Semiconductor CAAC-IGZO: Application to Displays

Shunpei Yamazaki and Tetsuo Tsutsui

OLED Displays: Fundamentals and Applications, Second Edition

Takatoshi Tsujimura

Physics and Technology of Crystalline Oxide Semiconductor CAAC-IGZO: Fundamentals

Noboru Kimizuka and Shunpei Yamazaki

Physics and Technology of Crystalline Oxide Semiconductor CAAC-IGZO: Application to LSI

Shunpei Yamazaki and Masahiro Fujita

Interactive Displays: Natural Human-Interface Techniques

Achintya K. Bhowmik

Addressing Techniques of Liquid Crystal Displays

Temkar N. Ruckmongathan

Modeling and Optimization of LCD Optical Performance

Dmitry A. Yakovlev, Vladimir G. Chigrinov, and Hoi-Sing Kwok

Fundamentals of Liquid Crystal Devices, Second Edition

Deng-Ke Yang and Shin-Tson Wu

3D Displays

Ernst Lueder

Illumination, Color and Imaging: Evaluation and Optimization of Visual Displays

P. Bodrogi and T. Q. Khan

Liquid Crystal Displays: Fundamental Physics and Technology

Robert H. Chen

Transflective Liquid Crystal Displays

Zhibing Ge and Shin-Tson Wu

LCD Backlights

Shunsuke Kobayashi, Shigeo Mikoshiba, and Sungkyoo Lim (Eds.)

Mobile Displays: Technology and Applications

Achintya K. Bhowmik, Zili Li, and Philip Bos (Eds.)

Photoalignment of Liquid Crystalline Materials: Physics and Applications

Vladimir G. Chigrinov, Vladimir M. Kozenkov, and Hoi-Sing Kwok

Projection Displays, Second Edition

Mathew S. Brennessoltz and Edward H. Stupp

Introduction to Microdisplays

David Armitage, Ian Underwood, and Shin-Tson Wu

Polarization Engineering for LCD Projection

Michael G. Robinson, Jianmin Chen, and Gary D. Sharp

Digital Image Display: Algorithms and Implementation

Gheorghe Berbecel

Colour Engineering: Achieving Device Independent Colour

Phil Green and Lindsay MacDonald (Eds.)

Display Interfaces: Fundamentals and Standards

Robert L. Myers

Reflective Liquid Crystal Displays

Shin-Tson Wu and Deng-Ke Yang

Display Systems: Design and Applications

Lindsay W. MacDonald and Anthony C. Lowe (Eds.)

Amorphous Oxide Semiconductors

IGZO and Related Materials for Display and Memory

Edited by

Hideo Hosono and Hideya Kumomi

Tokyo Institute of Technology, Japan

WILEY

This edition first published 2022
© 2022 John Wiley & Sons Ltd

All rights reserved. No part of this publication may be reproduced, stored in a retrieval system, or transmitted, in any form or by any means, electronic, mechanical, photocopying, recording or otherwise, except as permitted by law. Advice on how to obtain permission to reuse material from this title is available at <http://www.wiley.com/go/permissions>.

The right of Hideo Hosono and Hideya Kumomi to be identified as the authors of the editorial material in this work has been asserted in accordance with law.

Registered Offices

John Wiley & Sons, Inc., 111 River Street, Hoboken, NJ 07030, USA
John Wiley & Sons Ltd, The Atrium, Southern Gate, Chichester, West Sussex, PO19 8SQ, UK

Editorial Office

The Atrium, Southern Gate, Chichester, West Sussex, PO19 8SQ, UK

For details of our global editorial offices, customer services, and more information about Wiley products visit us at www.wiley.com.

Wiley also publishes its books in a variety of electronic formats and by print-on-demand. Some content that appears in standard print versions of this book may not be available in other formats.

Limit of Liability/Disclaimer of Warranty

While the publisher and authors have used their best efforts in preparing this work, they make no representations or warranties with respect to the accuracy or completeness of the contents of this work and specifically disclaim all warranties, including without limitation any implied warranties of merchantability or fitness for a particular purpose. No warranty may be created or extended by sales representatives, written sales materials or promotional statements for this work. The fact that an organization, website, or product is referred to in this work as a citation and/or potential source of further information does not mean that the publisher and authors endorse the information or services the organization, website, or product may provide or recommendations it may make. This work is sold with the understanding that the publisher is not engaged in rendering professional services. The advice and strategies contained herein may not be suitable for your situation. You should consult with a specialist where appropriate. Further, readers should be aware that websites listed in this work may have changed or disappeared between when this work was written and when it is read. Neither the publisher nor authors shall be liable for any loss of profit or any other commercial damages, including but not limited to special, incidental, consequential, or other damages.

Library of Congress Cataloging-in-Publication Data

Names: Hosono, Hideo, editor. | Kumomi, Hideya, editor.
Title: Amorphous oxide semiconductors : IGZO and related materials for display and memory / edited by Hideo Hosono and Hideya Kumomi, Tokyo Institute of Technology, Japan.
Other titles: Wiley SID series in display technology
Description: Hoboken, NJ : Wiley, 2022. | Series: Wiley-SID Series in Display Technology | Includes bibliographical references and index.
Identifiers: LCCN 2021052142 (print) | LCCN 2021052143 (ebook) | ISBN 9781119715573 (cloth) | ISBN 9781119715610 (adobe pdf) | ISBN 9781119715658 (epub)
Subjects: LCSH: Thin film transistors. | Indium gallium zinc oxide. | Amorphous semiconductors.
Classification: LCC TK7871.96.T45 A46 2022 (print) | LCC TK7871.96.T45 (ebook) | DDC 621.3815/28-dc23/eng/20211227
LC record available at <https://lcn.loc.gov/2021052142>
LC ebook record available at <https://lcn.loc.gov/2021052143>

Cover Design: Wiley
Cover Image: Courtesy of Hideya Kumomi

Set in 9.5/12.5pt STIXTwoText by Straive, Chennai, India

Contents

Preface	<i>xv</i>
Series Editor's Foreword	<i>xvii</i>
About the Editors	<i>xviii</i>
List of Contributors	<i>xix</i>

Part I Introduction 1

1.1	Transparent Amorphous Oxide Semiconductors for Display Applications	3
	<i>Hideo Hosono</i>	
1.1.1	Introduction to Amorphous Semiconductors as Thin-Film Transistor (TFT) Channels	3
1.1.2	Historical Overview	4
1.1.3	Oxide and Silicon	6
1.1.4	Transparent Amorphous Oxide Semiconductors	6
1.1.4.1	Electronic Structures	6
1.1.4.2	Materials	8
1.1.4.3	Characteristic Carrier Transport Properties	9
1.1.4.4	Electronic States	10
1.1.5	<i>P</i> -Type Oxide Semiconductors for Display Applications	13
1.1.5.1	Oxides of Transition Metal Cations with an Electronic Configuration of $(n-1)d^{10}ns^0$ ($n = 4$ or 5)	13
1.1.5.2	Oxides of Metal Cations with an Electronic Configuration of ns^2	13
1.1.5.3	Oxides of Metal Cations with an Electronic Configuration of nd^6	14
1.1.6	Novel Amorphous Oxide Semiconductors	15
1.1.7	Summary and Outlook	17
	References	18
1.2	Transparent Amorphous Oxide Semiconductors	21
	<i>Hideya Kumomi</i>	
1.2.1	Introduction	21
1.2.2	Technical Issues and Requirements of TFTs for AM-FPDs	21
1.2.2.1	Field-Effect Mobility	21
1.2.2.2	Off-State Leakage Current and On/Off Current Ratio	23
1.2.2.3	Stability and Reliability	23
1.2.2.4	Uniformity	23
1.2.2.5	Large-Area Devices by Large-Area Mother-Glass Substrates	24
1.2.2.6	Low-Temperature Fabrication and Flexibility	24
1.2.3	History, Features, Uniqueness, Development, and Applications of AOS-TFTs	24
1.2.3.1	History	24
1.2.3.2	Features and Uniqueness	25
1.2.3.3	Applications	27
1.2.3.4	Development and Products of AM-FPDs	28
1.2.4	Summary	29
	References	30

	Part II Fundamentals	31
2	Electronic Structure and Structural Randomness	33
	<i>Julia E. Medvedeva, Bishal Bhattarai, and D. Bruce Buchholz</i>	
2.1	Introduction	33
2.2	Brief Description of Methods and Approaches	35
2.2.1	Computational Approach	35
2.2.2	Experimental Approach	36
2.3	The Structure and Properties of Crystalline and Amorphous In_2O_3	36
2.4	The Structure and Properties of Crystalline and Amorphous SnO_2	43
2.5	The Structure and Properties of Crystalline and Amorphous ZnO	46
2.6	The Structure and Properties of Crystalline and Amorphous Ga_2O_3	52
2.7	Role of Morphology in Structure–Property Relationships	57
2.8	The Role of Composition in Structure–Property Relationships: IGO and IGZO	64
2.9	Conclusions	69
	References	70
3	Electronic Structure of Transparent Amorphous Oxide Semiconductors	73
	<i>John Robertson and Zhaofu Zhang</i>	
3.1	Introduction	73
3.2	Mobility	73
3.3	Density of States	74
3.4	Band Structures of n -Type Semiconductors	78
3.5	Instabilities	81
3.6	Doping Limits and Finding Effective Oxide Semiconductors	86
3.7	OLED Electrodes	88
3.8	Summary	89
	References	89
4	Defects and Relevant Properties	93
	<i>Toshio Kamiya, Kenji Nomura, Keisuke Ide, and Hideo Hosono</i>	
4.1	Introduction	93
4.2	Typical Deposition Condition	93
4.3	Overview of Electronic Defects in AOSs	94
4.4	Origins of Electron Donors	96
4.5	Oxygen- and Hydrogen-Related Defects and Near-VBM States	98
4.6	Summary	102
	References	102
5	Amorphous Semiconductor Mobility Physics and TFT Modeling	105
	<i>John F. Wager</i>	
5.1	Amorphous Semiconductor Mobility: An Introduction	105
5.2	Diffusive Mobility	106
5.3	Density of States	110
5.4	TFT Mobility Considerations	111
5.5	TFT Mobility Extraction, Fitting, and Model Validation	112
5.6	Physics-Based TFT Mobility Modeling	118
5.7	Conclusions	121
	References	122
6	Percolation Description of Charge Transport in Amorphous Oxide Semiconductors: Band Conduction Dominated by Disorder	125
	<i>A. V. Nenashev, F. Gebhard, K. Meerholz, and S. D. Baranovskii</i>	
6.1	Introduction	125
6.2	Band Transport via Extended States in the Random-Barrier Model (RBM)	126
6.2.1	Deficiencies of the Rate-Averaging Approach: Electrotechnical Analogy	127

6.2.2	Percolation Approach to Charge Transport in the RBM	129
6.3	Random Band-Edge Model (RBEM) for Charge Transport in AOSs	131
6.4	Percolation Theory for Charge Transport in the RBEM	133
6.4.1	From Regional to Global Conductivities in Continuum Percolation Theory	133
6.4.2	Averaging Procedure by Adler et al.	135
6.5	Comparison between Percolation Theory and EMA	136
6.6	Comparison with Experimental Data	137
6.7	Discussion and Conclusions	140
6.7.1	Textbook Description of Charge Transport in Traditional Crystalline Semiconductors (TCSs)	140
6.7.2	Results of This Chapter for Charge Transport in Amorphous Oxide Semiconductors (AOSs)	141
	Acknowledgments	141
	References	141
7	State and Role of Hydrogen in Amorphous Oxide Semiconductors	145
	<i>Hideo Hosono and Toshio Kamiya</i>	
7.1	Introduction	145
7.2	Concentration and Chemical States	145
7.3	Carrier Generation and Hydrogen	150
7.3.1	Carrier Generation by H Injection at Low Temperatures	150
7.3.2	Carrier Generation and Annihilation by Thermal Treatment	151
7.4	Energy Levels and Electrical Properties	153
7.5	Incorporation and Conversion of H Impurities	154
7.6	Concluding Remarks	155
	Acknowledgments	156
	References	156
	Part III Processing	159
8	Low-Temperature Thin-Film Combustion Synthesis of Metal-Oxide Semiconductors: Science and Technology	161
	<i>Binghao Wang, Wei Huang, Antonio Facchetti, and Tobin J. Marks</i>	
8.1	Introduction	161
8.2	Low-Temperature Solution-Processing Methodologies	162
8.2.1	Alkoxide Precursors	162
8.2.2	Microwave-Assisted Annealing	165
8.2.3	High-Pressure Annealing	165
8.2.4	Photonic Annealing	165
8.2.4.1	Laser Annealing	166
8.2.4.2	Deep-Ultraviolet Illumination	168
8.2.4.3	Flash Lamp Annealing	170
8.2.5	Redox Reactions	170
8.3	Combustion Synthesis for MO TFTs	171
8.3.1	<i>n</i> -Type MO TFTs	172
8.3.2	<i>p</i> -Type MO TFTs	178
8.4	Summary and Perspectives	180
	Acknowledgments	180
	References	181
9	Solution-Processed Metal-Oxide Thin-Film Transistors for Flexible Electronics	185
	<i>Hyun Jae Kim</i>	
9.1	Introduction	185
9.2	Fundamentals of Solution-Processed Metal-Oxide Thin-Film Transistors	187
9.2.1	Deposition Methods for Solution-Processed Oxide Semiconductors	187
9.2.1.1	Coating-Based Deposition Methods	190
9.2.1.2	Printing-Based Deposition Methods	191
9.2.2	The Formation Mechanism of Solution-Processed Oxide Semiconductor Films	194

- 9.3 Low-Temperature Technologies for Active-Layer Engineering of Solution-Processed Oxide TFTs 196
 - 9.3.1 Overview 196
 - 9.3.2 Solution Modulation 197
 - 9.3.2.1 Alkoxide Precursors 198
 - 9.3.2.2 pH Adjustment 199
 - 9.3.2.3 Combustion Reactions 199
 - 9.3.2.4 Aqueous Solvent 199
 - 9.3.3 Process Modulation 201
 - 9.3.3.1 Photoactivation Process 201
 - 9.3.3.2 High-Pressure Annealing (HPA) Process 202
 - 9.3.3.3 Microwave-Assisted Annealing Process 204
 - 9.3.3.4 Plasma-Assisted Annealing Process 204
 - 9.3.4 Structure Modulation 205
 - 9.3.4.1 Homojunction Dual-Active or Multiactive Layer 206
 - 9.3.4.2 Heterojunction Dual- or Multiactive Layer 206
- 9.4 Applications of Flexible Electronics with Low-Temperature Solution-Processed Oxide TFTs 208
 - 9.4.1 Flexible Displays 208
 - 9.4.2 Flexible Sensors 208
 - 9.4.3 Flexible Integrated Circuits 209
- References 209

10 Recent Progress on Amorphous Oxide Semiconductor Thin-Film Transistors Using the Atomic Layer Deposition Technique 213

Hyun-Jun Jeong and Jin-Seong Park

- 10.1 Atomic Layer Deposition (ALD) for Amorphous Oxide Semiconductor (AOS) Applications 213
 - 10.1.1 The ALD Technique 213
 - 10.1.2 Research Motivation for ALD AOS Applications 215
- 10.2 AOS-TFTs Based on ALD 217
 - 10.2.1 Binary Oxide Semiconductor TFTs Based on ALD 217
 - 10.2.1.1 ZnO-TFTs 217
 - 10.2.1.2 InOx-TFTs 218
 - 10.2.1.3 SnOx-TFTs 218
 - 10.2.2 Ternary and Quaternary Oxide Semiconductor TFTs Based on ALD 220
 - 10.2.2.1 Indium-Zinc Oxide (IZO) and Indium-Gallium Oxide (IGO) 220
 - 10.2.2.2 Zinc-Tin Oxide (ZTO) 223
 - 10.2.2.3 Indium-Gallium-Zinc Oxide (IGZO) 223
 - 10.2.2.4 Indium-Tin-Zinc Oxide (ITZO) 226
- 10.3 Challenging Issues of AOS Applications Using ALD 226
 - 10.3.1 *p*-Type Oxide Semiconductors 226
 - 10.3.1.1 Tin Monoxide (SnO) 228
 - 10.3.1.2 Copper Oxide (Cu_xO) 229
 - 10.3.2 Enhancing Device Performance: Mobility and Stability 230
 - 10.3.2.1 Composition Gradient Oxide Semiconductors 230
 - 10.3.2.2 Two-Dimensional Electron Gas (2DEG) Oxide Semiconductors 231
 - 10.3.2.3 Spatial and Atmospheric ALD for Oxide Semiconductors 234
- References 234

Part IV Thin-Film Transistors 239

11 Control of Carrier Concentrations in AOSs and Application to Bulk-Accumulation TFTs 241

Suhui Lee and Jin Jang

- 11.1 Introduction 241
- 11.2 Control of Carrier Concentration in *a*-IGZO 242
- 11.3 Effect of Carrier Concentration on the Performance of *a*-IGZO TFTs with a Dual-Gate Structure 247
 - 11.3.1 Inverted Staggered TFTs 247

11.3.2	Coplanar TFTs	251
11.4	High-Drain-Current, Dual-Gate Oxide TFTs	252
11.5	Stability of Oxide TFTs: PBTS, NBIS, HCTS, Hysteresis, and Mechanical Strain	259
11.6	TFT Circuits: Ring Oscillators and Amplifier Circuits	266
11.7	Conclusion	270
	References	270

12 Elevated-Metal Metal-Oxide Thin-Film Transistors: A Back-Gate Transistor Architecture with Annealing-Induced Source/Drain Regions 273

Man Wong, Zhihe Xia, and Jiapeng Li

12.1	Introduction	273
12.1.1	Semiconducting Materials for a TFT	274
12.1.1.1	Amorphous Silicon	274
12.1.1.2	Low-Temperature Polycrystalline Silicon	274
12.1.1.3	MO Semiconductors	275
12.1.2	TFT Architectures	276
12.2	Annealing-Induced Generation of Donor Defects	279
12.2.1	Effects of Annealing on the Resistivity of IGZO	279
12.2.2	Microanalyses of the Thermally Annealed Samples	283
12.2.3	Lateral Migration of the Annealing-Induced Donor Defects	284
12.3	Elevated-Metal Metal-Oxide (EMMO) TFT Technology	286
12.3.1	Technology and Characteristics of IGZO EMMO TFTs	287
12.3.2	Applicability of EMMO Technology to Other MO Materials	291
12.3.3	Fluorinated EMMO TFTs	292
12.3.4	Resilience of Fluorinated MO against Hydrogen Doping	296
12.3.5	Technology and Display Resolution Trend	298
12.4	Enhanced EMMO TFT Technologies	301
12.4.1	3-EMMO TFT Technology	302
12.4.2	Self-Aligned EMMO TFTs	307
12.5	Conclusion	309
	Acknowledgments	310
	References	310

13 Hot Carrier Effects in Oxide-TFTs 315

Mami N. Fujii, Takanori Takahashi, Juan Paolo Soria Bermundo, and Yukiharu Uraoka

13.1	Introduction	315
13.2	Analysis of Hot Carrier Effect in IGZO-TFTs	315
13.2.1	Photoemission from IGZO-TFTs	315
13.2.2	Kink Current in Photon Emission Condition	318
13.2.3	Hot Carrier-Induced Degradation of <i>a</i> -IGZO-TFTs	318
13.3	Analysis of the Hot Carrier Effect in High-Mobility Oxide-TFTs	322
13.3.1	Bias Stability under DC Stresses in a High-Mobility IWZO-TFT	322
13.3.2	Analysis of Dynamic Stress in Oxide-TFTs	323
13.3.3	Photon Emission from the IWZO-TFT under Pulse Stress	323
13.4	Conclusion	328
	References	328

14 Carbon-Related Impurities and NBS Instability in AOS-TFTs 333

Junghwan Kim and Hideo Hosono

14.1	Introduction	333
14.2	Experimental	334
14.3	Results and Discussion	334
14.4	Summary	337
	References	339

	Part V TFTs and Circuits	341
15	Oxide TFTs for Advanced Signal-Processing Architectures	343
	<i>Arokia Nathan, Denis Striakhilev, and Shuenn-Jiun Tang</i>	
15.1	Introduction	343
15.1.1	Device–Circuit Interactions	343
15.2	Above-Threshold TFT Operation and Defect Compensation: AMOLED Displays	345
15.2.1	AMOLED Display Challenges	345
15.2.2	Above-Threshold Operation	347
15.2.3	Temperature Dependence	347
15.2.4	Effects of Process-Induced Spatial Nonuniformity	349
15.2.5	Overview of External Compensation for AMOLED Displays	351
15.3	Ultralow-Power TFT Operation in a Deep Subthreshold (Near Off-State) Regime	354
15.3.1	Schottky Barrier TFTs	355
15.3.2	Device Characteristics and Small Signal Parameters	358
15.3.3	Common Source Amplifier	360
15.4	Oxide TFT-Based Image Sensors	362
15.4.1	Heterojunction Oxide Photo-TFTs	362
15.4.2	Persistent Photocurrent	364
15.4.3	All-Oxide Photosensor Array	365
	References	366
16	Device Modeling and Simulation of TAOS-TFTs	369
	<i>Katsumi Abe</i>	
16.1	Introduction	369
16.2	Device Models for TAOS-TFTs	369
16.2.1	Mobility Model	369
16.2.2	Density of Subgap States (DOS) Model	371
16.2.3	Self-Heating Model	372
16.3	Applications	373
16.3.1	Temperature Dependence	373
16.3.2	Channel-Length Dependence	373
16.3.3	Channel-Width Dependence	375
16.3.4	Dual-Gate Structure	378
16.4	Reliability	379
16.5	Summary	381
	Acknowledgments	381
	References	382
17	Oxide Circuits for Flexible Electronics	383
	<i>Kris Myny, Nikolaos Papadopoulos, Florian De Roose, and Paul Heremans</i>	
17.1	Introduction	383
17.2	Technology-Aware Design Considerations	383
17.2.1	Etch-Stop Layer, Backchannel Etch, and Self-Aligned Transistors	384
17.2.1.1	Etch-Stop Layer	384
17.2.1.2	Backchannel Etch	385
17.2.1.3	Self-Aligned Transistors	385
17.2.1.4	Comparison	386
17.2.2	Dual-Gate Transistors	386
17.2.2.1	Stack Architecture	386
17.2.2.2	Effect of the Backgate	388
17.2.3	Moore’s Law for TFT Technologies	389
17.2.3.1	CMOS	389

17.2.3.2	Thin-Film Electronics Historically	389
17.2.3.3	New Drivers for Thin-Film Scaling: Circuits	390
17.2.3.4	L-Scaling	391
17.2.3.5	W and L Scaling	391
17.2.3.6	Overall Lateral Scaling	391
17.2.3.7	Oxide Thickness and Supply Voltage Scaling	391
17.2.4	Conclusion	392
17.3	Digital Electronics	392
17.3.1	Communication Chips	392
17.3.2	Complex Metal-Oxide-Based Digital Chips	395
17.4	Analog Electronics	396
17.4.1	Thin-Film ADC Topologies	396
17.4.2	Imager Readout Peripherals	397
17.4.3	Healthcare Patches	399
17.5	Summary	400
	Acknowledgments	400
	References	400

Part VI Display and Memory Applications 405

18 Oxide TFT Technology for Printed Electronics 407

Toshiaki Arai

18.1	OLEDs	407
18.1.1	OLED Displays	407
18.1.2	Organic Light-Emitting Diodes	408
18.1.3	Printed OLEDs	409
18.2	TFTs for OLED Driving	413
18.2.1	TFT Candidates	413
18.2.2	Pixel Circuits	413
18.2.3	Oxide TFTs	414
18.2.3.1	Bottom-Gate TFTs	415
18.2.3.2	Top-Gate TFTs	418
18.3	Oxide TFT-Driven Printed OLED Displays	424
18.4	Summary	427
	References	428

19 Mechanically Flexible Nonvolatile Memory Thin-Film Transistors Using Oxide Semiconductor Active Channels on Ultrathin Polyimide Films 431

Sung-Min Yoon, Hyeong-Rae Kim, Hye-Won Jang, Ji-Hee Yang, Hyo-Eun Kim, and Sol-Mi Kwak

19.1	Introduction	431
19.2	Fabrication of Memory TFTs	432
19.2.1	Substrate Preparation	432
19.2.2	Device Fabrication Procedures	434
19.2.3	Characterization Methodologies	435
19.3	Device Operations of Flexible Memory TFTs	437
19.3.1	Optimization of Flexible IGZO-TFTs on PI Films	437
19.3.2	Nonvolatile Memory Operations of Flexible Memory TFTs	438
19.3.3	Operation Mechanisms and Device Physics	442
19.4	Choice of Alternative Materials	444
19.4.1	Introduction to Conducting Polymer Electrodes	444
19.4.2	Introduction of Polymeric Gate Insulators	446
19.5	Device Scaling to Vertical-Channel Structures	447

19.5.1	Vertical-Channel IGZO-TFTs on PI Films	447
19.5.2	Vertical-Channel Memory TFTs Using IGZO Channel and ZnO Trap Layers	449
19.6	Summary	453
19.6.1	Remaining Technical Issues	453
19.6.2	Conclusions and Outlooks	453
	References	454
20	Amorphous Oxide Semiconductor TFTs for BEOL Transistor Applications	457
	<i>Nobuyoshi Saito and Keiji Ikeda</i>	
20.1	Introduction	457
20.2	Improvement of Immunity to H ₂ Annealing	458
20.3	Increase of Mobility and Reduction of S/D Parasitic Resistance	463
20.4	Demonstration of Extremely Low Off-State Leakage Current Characteristics	467
	References	471
21	Ferroelectric-HfO₂ Transistor Memory with IGZO Channels	473
	<i>Masaharu Kobayashi</i>	
21.1	Introduction	473
21.2	Device Operation and Design	475
21.3	Device Fabrication	478
21.4	Experimental Results and Discussions	479
21.4.1	FE-HfO ₂ Capacitors with an IGZO Layer	479
21.4.2	IGZO Channel FeFETs	481
21.5	Summary	484
	Acknowledgments	484
	References	485
22	Neuromorphic Chips Using AOS Thin-Film Devices	487
	<i>Mutsumi Kimura</i>	
22.1	Introduction	487
22.2	Neuromorphic Systems with Crosspoint-Type α -GTO Thin-Film Devices	488
22.2.1	Neuromorphic Systems	488
22.2.1.1	α -GTO Thin-Film Devices	488
22.2.1.2	System Architecture	489
22.2.2	Experimental Results	492
22.3	Neuromorphic System Using an LSI Chip and α -IGZO Thin-Film Devices [24]	493
22.3.1	Neuromorphic System	494
22.3.1.1	Neuron Elements	494
22.3.1.2	Synapse Elements	494
22.3.1.3	System Architecture	495
22.3.2	Working Principle	495
22.3.2.1	Cellular Neural Network	495
22.3.2.2	Tug-of-War Method	497
22.3.2.3	Modified Hebbian Learning	497
22.3.2.4	Majority-Rule Handling	498
22.3.3	Experimental Results	498
22.3.3.1	Raw Data	498
22.3.3.2	Associative Memory	499
22.4	Conclusion	499
	Acknowledgments	500
	References	500

23	Oxide TFTs and Their Application to X-Ray Imaging	503
	<i>Robert A. Street</i>	
23.1	Introduction	503
23.2	Digital X-Ray Detection and Imaging Modalities	504
23.2.1	Indirect Detection Imaging	504
23.2.2	Direct Detection Imaging	505
23.2.3	X-Ray Imaging Modalities	505
23.3	Oxide-TFT X-Ray Detectors	506
23.3.1	TFT Backplane Requirements for Digital X-Rays	506
23.3.2	An IGZO Detector Fabrication and Characterization	506
23.3.3	Other Reported Oxide X-Ray Detectors	509
23.4	How Oxide TFTs Can Improve Digital X-Ray Detectors	509
23.4.1	Noise and Image Quality in X-Ray Detectors	510
23.4.2	Minimizing Additive Electronic Noise with Oxides	510
23.4.3	Pixel Amplifier Backplanes	511
23.4.4	IGZO-TFT Noise	511
23.5	Radiation Hardness of Oxide TFTs	513
23.6	Oxide Direct Detector Materials	515
23.7	Summary	515
	References	515
	Part VII New Materials	519
24	Toward the Development of High-Performance <i>p</i>-Channel Oxide-TFTs and All-Oxide Complementary Circuits	521
	<i>Kenji Nomura</i>	
24.1	Introduction	521
24.2	Why Is High-Performance <i>p</i> -Channel Oxide Difficult?	521
24.3	The Current Development of <i>p</i> -Channel Oxide-TFTs	524
24.4	Comparisons of <i>p</i> -Type Cu ₂ O and SnO Channels	526
24.5	Comparisons of the TFT Characteristics of Cu ₂ O and SnO-TFTs	529
24.6	Subgap Defect Termination for <i>p</i> -Channel Oxides	532
24.7	All-Oxide Complementary Circuits	534
24.8	Conclusions	535
	References	536
25	Solution-Synthesized Metal Oxides and Halides for Transparent <i>p</i>-Channel TFTs	539
	<i>Ao Liu, Huihui Zhu, and Yong-Young Noh</i>	
25.1	Introduction	539
25.2	Solution-Processed <i>p</i> -Channel Metal-Oxide TFTs	540
25.3	Transparent Copper(I) Iodide (CuI)-Based TFTs	546
25.4	Conclusions and Perspectives	548
	Acknowledgments	549
	References	549
26	Tungsten-Doped Active Layers for High-Mobility AOS-TFTs	553
	<i>Zhang Qun</i>	
26.1	Introduction	553
26.2	Advances in Tungsten-Doped High-Mobility AOS-TFTs	555
26.2.1	α -IWO-TFTs	555

- 26.2.2 α -IZWO-TFTs 562
- 26.2.3 Dual Tungsten-Doped Active-Layer TFTs 565
- 26.2.4 Treatment on the Backchannel Surface 566
- 26.3 Perspectives for High-Mobility AOS Active Layers 570
- References 572

- 27 Rare Earth- and Transition Metal-Doped Amorphous Oxide Semiconductor Phosphors for Novel Light-Emitting Diode Displays 577**
Keisuke Ide, Junghwan Kim, Hideo Hosono, and Toshio Kamiya
- 27.1 Introduction 577
- 27.2 Eu-Doped Amorphous Oxide Semiconductor Phosphor 577
- 27.3 Multiple-Color Emissions from Various Rare Earth-Doped AOS Phosphors 579
- 27.4 Transition Metal-Doped AOS Phosphors 582
- References 584

- 28 Application of AOSs to Charge Transport Layers in Electroluminescent Devices 585**
Junghwan Kim and Hideo Hosono
- 28.1 Electronic Structure and Electrical Properties of Amorphous Oxide Semiconductors (AOSs) 585
- 28.2 Criteria for Charge Transport Layers in Electroluminescent (EL) Devices 585
- 28.3 Amorphous Zn-Si-O Electron Transport Layers for Perovskite Light-Emitting Diodes (PeLEDs) 587
- 28.4 Amorphous In-Mo-O Hole Injection Layers for OLEDs 589
- 28.5 Perspective 594
- References 595

- 29 Displays and Vertical-Cavity Surface-Emitting Lasers 597**
Kenichi Iga
- 29.1 Introduction to Displays 597
- 29.2 Liquid Crystal Displays (LCDs) 597
- 29.2.1 History of LCDs 597
- 29.2.2 Principle of LCD: The TN Mode 598
- 29.2.3 Other LC Modes 600
- 29.2.4 Light Sources 600
- 29.2.5 Diffusion Plate and Light Guiding Layer 601
- 29.2.6 Microlens Arrays 601
- 29.2.7 Short-Focal-Length Projection 602
- 29.3 Organic EL Display 602
- 29.3.1 Method (a): Color-Coding Method 603
- 29.3.2 Method (b): Filter Method 603
- 29.3.3 Method (c): Blue Conversion Method 603
- 29.4 Vertical-Cavity Surface-Emitting Lasers 604
- 29.4.1 Motivation of Invention 604
- 29.4.2 What Is the Difference? 605
- 29.4.3 Device Realization 605
- 29.4.4 Applications 607
- 29.5 Laser Displays including VCSELs 607
- 29.5.1 Laser Displays 607
- 29.5.2 Color Gamut 608
- 29.5.3 Laser Backlight Method 609
- Acknowledgments 610
- References 611

Preface

The Fermi level can be controlled in semiconductors via impurity doping or by applying an electric field. Amorphous materials have distinct advantages over their crystalline counterparts in terms of processability and homogeneity (i.e., ease of fabrication of large-sized homogeneous thin films at low temperatures). Amorphous materials with good controllability of their Fermi level would be highly beneficial for large-area electronics, optoelectronics, and flexible applications. These advantages are the major driving force for researching amorphous semiconductors. However, controlling the Fermi level in amorphous semiconductors is impossible because of high-density carrier traps arising from structural randomness. An exception is hydrogenated amorphous silicon (a-Si:H), which is widely used in solar cells and thin-film transistors (TFTs) for liquid crystal displays (LCDs). However, band conduction has not been attained in a-Si:H. Thus, the mobility of a-Si:H remains at $\sim 1 \text{ cm}^2/\text{Vs}$, which is less than that of polycrystalline Si by two orders of magnitude.

Transparent amorphous oxide semiconductors (TAOSs) are a novel class of amorphous semiconductors characterized by their ionic bonding nature. In addition to high optical transparency to visible light, their mobility is greater than that of a-Si:H by one order of magnitude and can be fabricated using conventional direct current (DC) sputtering at low temperatures. Presently, TFTs with a channel layer of In-Ga-Zn-O (IGZO) are used to drive pixels of high-definition and energy-saving LCDs in smartphones, tablets, PC monitors, and large-sized organic light-emitting diode (OLED) TVs, and they are being studied for several more applications in X-ray imagers and memory devices.

Although materials science and device physics of TAOS have rapidly advanced in the last decade, the understanding of science and technology is incomplete due to the short research history and the difference in chemical bonding between oxides and covalent-type semiconductors. Consequently, conventional processing used for a-Si:H has caused serious degradation of the resulting devices, such as plasma treatment involving hydrogen. TAOS is the only semiconducting material that can be fabricated by heating the precursor in the ambient atmosphere. Solution-derived processing has been extensively studied for using this unique feature for flexible electronics.

This monograph provides a current understanding of amorphous oxide semiconductors with high mobility and their application to electronics, especially TFTs for displays. The book presents introductory fundamentals and discussions on TFTs and processing, circuits and device simulations, applications to displays and memory devices, and new materials. The authors of each chapter are experts with distinct research achievements in their subject area, and they describe state-of-the-art information along with some fundamental prerequisites for understanding. For further study, some review articles and books are listed in the references.

Notwithstanding that the research history of TAOS and their TFT applications is rather short, they now lead the backplane of advanced displays, with applications to memory devices and imagers soon to begin. Furthermore, application to flexible electronics is expected to employ low-temperature processability. Unfortunately, no monograph on TAOSs and TAOS-TFTs has been published to date. I intend to fill the gap between rapid research progress in this field and the demand for relevant semiconductors and devices by researchers, engineers, and students. The background of this book was the 77th Fujihara Seminar held in Hakone, Japan, in October 2019. We appreciate

the financial support from the Fujihara Foundation of Science and the contributors for presenting wonderful talks and active discussions.

The planning of this book was first solicited by Dr. Ian Underwood, the publication committee chair of the Society for Information Display (SID). I appreciate his guidance and patience. I acknowledge my colleagues at Tokyo Tech for organizing the seminar and editing this book. Special thanks to Professors Hideya Kumomi, Junghwan Kim, and Keisuke Ide. Finally, I dedicate this monograph to Dr. Kazunobu Tanaka, a pioneer in amorphous semiconductors. When I was a PhD candidate, I was impressed by his enthusiastic talk on photostructural change in amorphous chalcogenide. I am happy to be presented with the opportunity to publish this book on a novel class of amorphous semiconductors with excellent colleagues.

June 2021

Hideo Hosono
Tokyo Institute of Technology

Series Editor's Foreword

Within the flat-panel display industry, most technological change has occurred in an incremental and evolutionary manner, where developments in materials, processes, and precision have gradually improved products to provide the outstanding performance and capability we see today. Against this background, there have been a small number of truly revolutionary innovations; the adoption of in-plane inductor–capacitor (LC) switching modes and the introduction of organic light-emitting devices (OLEDs) provide examples in which a complete redesign of the display was needed, which in turn provided outstanding advantages in panel performance.

Among these revolutionary changes, the use of transparent oxide semiconductors in place of amorphous or polycrystalline silicon in active-matrix (AM) backplanes has been one of the most dramatic. Although oxide semiconductors have been known and studied for many decades, their use in thin-film transistor (TFT) channels was regarded as impractical before the advances in understanding and materials design that were achieved toward the end of the twentieth century. Once the underlying science was established, the pace at which these novel materials have been introduced into a wide range of commercial products is exceptional. The lead editor of this volume, Professor Hosono, may be regarded as the father of this renaissance in oxide semiconductor technology, due to his decisive contributions to the basic science, technology, and exploitation of new oxide materials. Now, oxide TFTs offer many advantages; they can be fabricated at low temperature and without costly laser annealing, while their high mobility provides routes to higher-resolution displays, faster frame rates, and higher optical power efficiency. The wide bandgap of oxide systems promotes extremely low leakage currents and allows fabrication of transparent TFT arrays. The impact of oxide backplanes on the user's experience of modern displays is also profound, including a leap forward in image quality combined in many cases with reduced power drain.

The development of this new semiconductor class has brought many difficulties, some of which have been overcome while others continue to provide challenges and opportunities to the community. Among the outstanding issues, the difficulty of obtaining high performance in p-type oxide channels is of greater importance, as oxide devices are applied to more complex circuitry for memory, logic, and processing tasks outside the display driver array. Nevertheless, the advantages of oxide devices make such “system-on-panel” integration highly attractive. In the present volume, the editors, Professors Hosono and Hideya Kumomi, have brought together a comprehensive and authoritative collection of contributions from leading scientists in the field, which cover all the important topics touching advanced oxide semiconductors—materials design, electronic properties, characterization and modeling, device design, performance and stability, systems integration, new applications, and the challenges of applying oxide components to new-generation devices on plastic and other flexible substrates. The chapters go beyond the well-established applications of oxide systems to critically examine remaining challenges, such as prospects for oxide-based complementary metal-oxide semiconductors (CMOSs) and alternative circuit architectures as well as applications of oxide to other large-area electronic applications.

The trend to use oxide backplanes in displays is set to accelerate and broaden into new application areas that will place more and more stringent demands on AM components and their peripherals. Oxide TFTs will also find increased use in nondisplay devices. As these trends develop, this book will provide a ready and invaluable source of reference for all those studying, applying, and exploiting oxide semiconductors.

About the Editors

Hideo Hosono is an honorary professor and the founding director of the Materials Research Center for Element Strategy (MCES) of Tokyo Institute of Technology, and a distinguished fellow of the National Institute of Materials Science (NIMS). He is well known as a pioneer of transparent oxide semiconductors, iron-based superconductors, and inorganic electride materials. His proposal of a materials design concept for transparent amorphous oxide semiconductors with high electron mobility in 1995 and his demonstration of the first thin-film transistor (TFT) of crystalline (2003) and amorphous indium–gallium–zinc oxide (IGZO) are milestones in this field. He is a recipient of the Jan Raychman Prize (Society for Information Display [SID]), the von Hippel Prize (Materials Research Society [MRS]), the James C. McGroddy Prize (American Physical Society [APS]), and the Japan Prize, and he is a fellow of the SID and the Royal Society of London. He was awarded a PhD by Tokyo Metropolitan University in 1982.

Hideya Kumomi is a specially appointed professor of the Materials Research Center for Element Strategy (MCS) of Tokyo Institute of Technology, and a program manager of the Tokodai Institute for Element Strategy. He had been in industry for a quarter of a century working on silicon-based semiconductor technologies, and then switched to oxide semiconductor technologies for thin-film transistors. Since joining academia, he has managed a national project called the Element Strategy Initiative in Japan. He received his PhD from Waseda University in 1996.

List of Contributors

Katsumi Abe

Silvaco Japan
Yokohama, Japan

Toshiaki Arai

JOLED
Kyoto, Japan

S. D. Baranovskii

Department of Physics and
Material Sciences Center
Philipps-University
Marburg, Germany
and

Department of Chemistry
University of Cologne
Cologne, Germany

Juan Paolo Soria Bermundo

Graduate School of Science and Technology
Nara Institute of Science and Technology
Ikoma, Japan

Bishal Bhattarai

Department of Physics
Missouri University of Science and Technology
Rolla, Missouri, USA

D. Bruce Buchholz

Department of Materials Science and Engineering
Northwestern University
Evanston, Illinois, USA

Florian De Roose

Sense and Actuate Technologies Department
imec
Heverlee, Belgium

Antonio Facchetti

Department of Chemistry and
Materials Research Center
Northwestern University
and
Evanston, Illinois, USA
Flexterra
Skokie, Illinois, USA

Mami N. Fujii

Graduate School of Science and Technology
Nara Institute of Science and Technology
Ikoma, Japan

F. Gebhard

Department of Physics and
Material Sciences Center
Philipps-University
Marburg, Germany

Paul Heremans

Sense and Actuate Technologies Department
imec
Heverlee, Belgium
and
Department of Electrical Engineering (ESAT)
KU Leuven
Leuven, Belgium

Hideo Hosono

Laboratory for Materials and Structures and
Materials Research Center for Element Strategy
Tokyo Institute of Technology
Yokohama, Japan
and
National Institute for Materials Research
Tsukuba, Japan

Wei Huang

Joint International Research Laboratory of
Information Display and Visualization
Key Laboratory of MEMS of Ministry of Education
School of Electronic Science and Engineering
Southeast University
Nanjing, China

Keisuke Ide

Laboratory for Materials and Structures
Tokyo Institute of Technology
Yokohama, Japan

Kenichi Iga

Laboratory for Future Interdisciplinary Research of
Science and Technology (FIRST)
Tokyo Institute of Technology
Yokohama, Japan

Keiji Ikeda

KIOXIA
Tokyo, Japan

Hye-Won Jang

Department of Advanced Materials Engineering for
Information and Electronics
Kyung Hee University
Seoul, Republic of Korea

Jin Jang

Advanced Display Research Center (ADRC)
Department of Information Display
Kyung Hee University
Seoul, Republic of Korea

Hyun-Jun Jeong

Division of Material Science and Engineering
Hanyang University

Seoul, Republic of Korea

Toshio Kamiya

Laboratory for Materials and Structures and
Materials Research Center for Element Strategy
Tokyo Institute of Technology
Yokohama, Japan

Hyeong-Rae Kim

Department of Advanced Materials Engineering for
Information and Electronics
Kyung Hee University
Seoul, Republic of Korea

Hyo-Eun Kim

Department of Advanced Materials Engineering for
Information and Electronics
Kyung Hee University
Seoul, Republic of Korea

Hyun Jae Kim

School of Electrical and Electronic Engineering
Yonsei University
Seoul, Republic of Korea

Junghwan Kim

Materials Research Center for Element Strategy
Tokyo Institute of Technology
Yokohama, Japan

Mutsumi Kimura

Ryukoku University
Kyoto, Japan
and
Nara Institute of Science and Technology
Ikoma, Japan

Masaharu Kobayashi

d.lab Systems Design Lab
School of Engineering
The University of Tokyo
Tokyo, Japan

Hideya Kumomi

Materials Research Center for Element Strategy
Tokyo Institute of Technology
Yokohama, Japan

Sol-Mi Kwak

Department of Advanced Materials Engineering for
Information and Electronics
Kyung Hee University
Seoul, Republic of Korea

Suhui Lee

Advanced Display Research Center (ADRC)
Department of Information Display
Kyung Hee University
Seoul, Republic of Korea

Jiapeng Li

Department of Electronic and Computer
Engineering and
State Key Laboratory of Advanced Displays
and Optoelectronics Technologies
The Hong Kong University of Science and Technology
Hong Kong, China

Ao Liu

Department of Chemical Engineering
Pohang University of Science and Technology
Pohang, Republic of Korea

Tobin J. Marks

Department of Chemistry and
Materials Research Center
Northwestern University
Evanston, Illinois, USA

Julia E. Medvedeva

Department of Physics
Missouri University of Science and Technology
Rolla, Missouri, USA

K. Meerholz

Department of Chemistry
University of Cologne
Cologne, Germany

Kris Myny

Sense and Actuate Technologies Department
imec
Heverlee, Belgium
and
Department of Electrical Engineering (ESAT)
KU Leuven
Leuven, Belgium

Arokia Nathan

Darwin College
University of Cambridge
Cambridge, UK

A. V. Nenashev

Institute of Semiconductor Physics
Novosibirsk, Russia
and
Department of Physics
Novosibirsk State University
Novosibirsk, Russia

Yong-Young Noh

Department of Chemical Engineering
Pohang University of Science and Technology
Pohang, Republic of Korea

Kenji Nomura

Department of Electrical and Computer Engineering
University of California, San Diego
La Jolla, California, USA

Nikolaos Papadopoulos

Sense and Actuate Technologies Department
imec
Heverlee, Belgium

Jin-Seong Park

Division of Material Science and Engineering
Hanyang University
Seoul, Republic of Korea

Zhang Qun

Department of Materials Science
Fudan University
Shanghai, China

John Robertson

Engineering Department
Cambridge University
Cambridge, UK

Nobuyoshi Saito

KIOXIA
Tokyo, Japan

Robert A. Street

Palo Alto Research Center
Palo Alto, California, USA

Denis Striakhilev

Ignis Innovation
Waterloo, Ontario, Canada

Takanori Takahashi

Graduate School of Science and Technology
Nara Institute of Science and Technology
Ikoma, Japan

Shuenn-Jiun Tang

Ignis Innovation
Waterloo, Ontario, Canada

Yukiharu Uraoka

Graduate School of Science and Technology
Nara Institute of Science and Technology
Ikoma, Japan

John F. Wager

School of Electrical Engineering and Computer
Science (EECS)
Oregon State University
Corvallis, Oregon, USA

Binghao Wang

Joint International Research Laboratory of
Information Display and Visualization
Key Laboratory of MEMS of Ministry of Education
School of Electronic Science and Engineering
Southeast University
Nanjing, China

and

Department of Chemistry and
Materials Research Center
Northwestern University
Evanston, Illinois, USA

Man Wong

Department of Electronic and Computer
Engineering and
State Key Laboratory of Advanced Displays and
Optoelectronics Technologies
The Hong Kong University of Science and Technology
Hong Kong, China

Zhihe Xia

Department of Electronic and Computer
Engineering and
State Key Laboratory of Advanced Displays and
Optoelectronics Technologies
The Hong Kong University of Science and Technology
Hong Kong, China

Ji-Hee Yang

Department of Advanced Materials Engineering for
Information and Electronics
Kyung Hee University
Seoul, Republic of Korea

Sung-Min Yoon

Department of Advanced Materials Engineering for
Information and Electronics
Kyung Hee University
Seoul, Republic of Korea

Zhaofu Zhang

Engineering Department
Cambridge University
Cambridge, UK

Huihui Zhu

Department of Chemical Engineering
Pohang University of Science and Technology
Pohang, Republic of Korea

Part I

Introduction

1.1

Transparent Amorphous Oxide Semiconductors for Display Applications

Materials, Features, Progress, and Prospects

Hideo Hosono

*Material Research Center for Element Strategy, Tokyo Institute of Technology, Tokyo, Japan
National Institute for Materials Research, Tsukuba, Japan*

1.1.1 Introduction to Amorphous Semiconductors as Thin-Film Transistor (TFT) Channels

Condensed matter is classified into two categories, crystalline and amorphous materials, depending on whether a unit cell exists or not. This discrimination is performed by X-ray diffraction. Amorphous materials have several distinct advantages over crystalline materials. Large-sized and homogeneous (grain-boundary-free) thin films can be easily fabricated at low temperatures. In addition, material properties may be tuned by varying the chemical composition because there is no limitation to compound formations.

The essence of semiconductors is controllability of the Fermi level (E_F) by intentional operations such as impurity doping and biasing. If the advantage of amorphous materials and the essence of semiconductors could be merged, the resulting amorphous semiconductor should be an ideal semiconductor for giant microelectronics represented by flat-panel displays, as illustrated in Figure 1.1.1.

However, the amorphous semiconductors reported so far are far from this ideal owing to the high concentration of defects (chemical disorders) and tail states (localized states induced by structural randomness). Figure 1.1.2 shows a schematic drawing of electronic states. Since these defects and tail states work as charge-trapping sites, control of the Fermi level is generally impossible in amorphous semiconductors. As a consequence, charge transport is restricted to hopping among localized state like amorphous chalcogenides and semiconducting oxide glasses based on V_2O_5 . The requirements for semiconductor thin-film transistor (TFT) channels are rather severe compared with the conventional semiconducting nature. Although these amorphous semiconductors do not work as TFT channels due to their high localized state density, amorphous hydrogenated Si (a-Si:H) is the first amorphous semiconductor in which E_F is controllable by biasing. This is the primary reason why a-Si:H has attracted much attention. A large reduction of dangling bonds giving a midgap level by passivation with hydrogen makes it possible to shift E_F to band edges, but E_F cannot exceed mobility edges. Thus, the mobility of a-Si:H TFTs remains $0.5\text{--}1\text{ cm}^2/(\text{Vs})$, which is lower by two orders of magnitude than that of polycrystalline Si-TFTs.

Transparent amorphous oxide semiconductors (TAOSs) based on post transition metal (PTM) oxides are the first category of amorphous semiconductors in which E_F is controllable beyond the mobility edge in the conduction band. As a result, TAOS-TFTs exhibit large mobility, $>10\text{ cm}^2/(\text{Vs})$, which is comparable to that in the corresponding polycrystalline thin films. What is the origin of such a favorable property of TAOSs? This is one focus of this chapter.

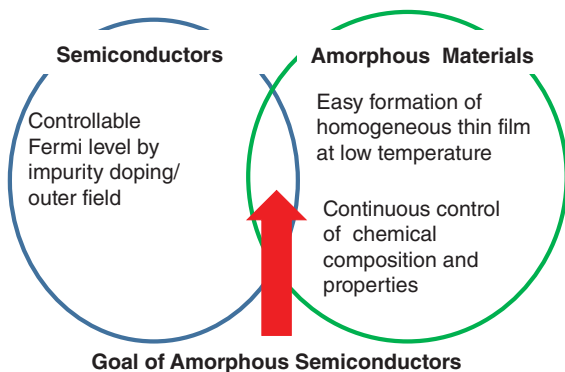


Figure 1.1.1 Ideal amorphous semiconductors.

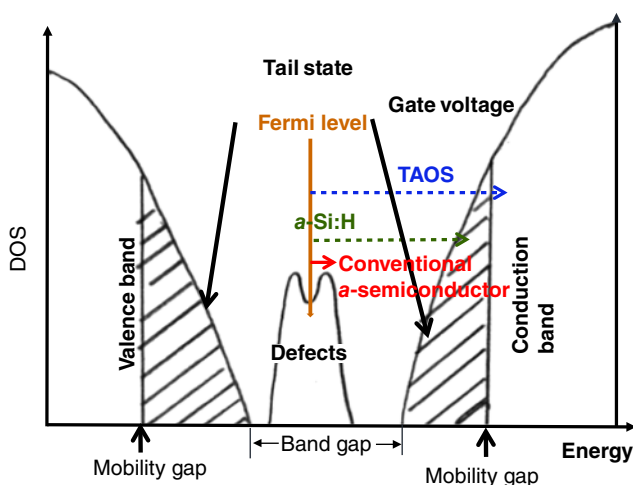


Figure 1.1.2 Electronic structure of amorphous semiconductors and material-dependent Fermi level controllability by biasing gate voltage.

1.1.2 Historical Overview

The history of oxide semiconductors is rather long. Transition metal-based oxides were traditional semiconductors, and so many papers on this topic have been published to date. However, as far as the author knows, neither of them works as the channel layer of TFTs. Transition metal cations have an open-shell structure in their d orbitals and give visible absorption originating from a $d-d$ transition. Since these vacant d levels give large densities of states (DOSS) in the gap, it is hard to shift the E_F to significantly exceed these DOSSs. This is the reason why transition metal-oxide semiconductors do not work as TFTs. As described in Section 1.1.1, requirements for semiconductors in TFT channels are much more severe than those for $p-n$ junction formation, because the E_F is needed to shift to valence band maximum (VBM) or conduction band maximum (CBM) by gate voltage. A representative example is Cu_2O , which is well known as a p -type semiconductor with high Hall mobility ($\sim 100 \text{ cm}^2/\text{Vs}$), but its TFT has not operated well (even now) since the first attempt by William Shockley in 1949.

Figure 1.1.3 summarizes the history of oxide TFTs and their relevant TFT technology. The first TFT device structure was proposed in 1926 by Julius Lilienfeld as a patent. Oxide semiconductor TFTs have a long history comparable to that of Si metal-oxide semiconductor field-effect transistors (MOSFETs). In the 1960s, the field effects

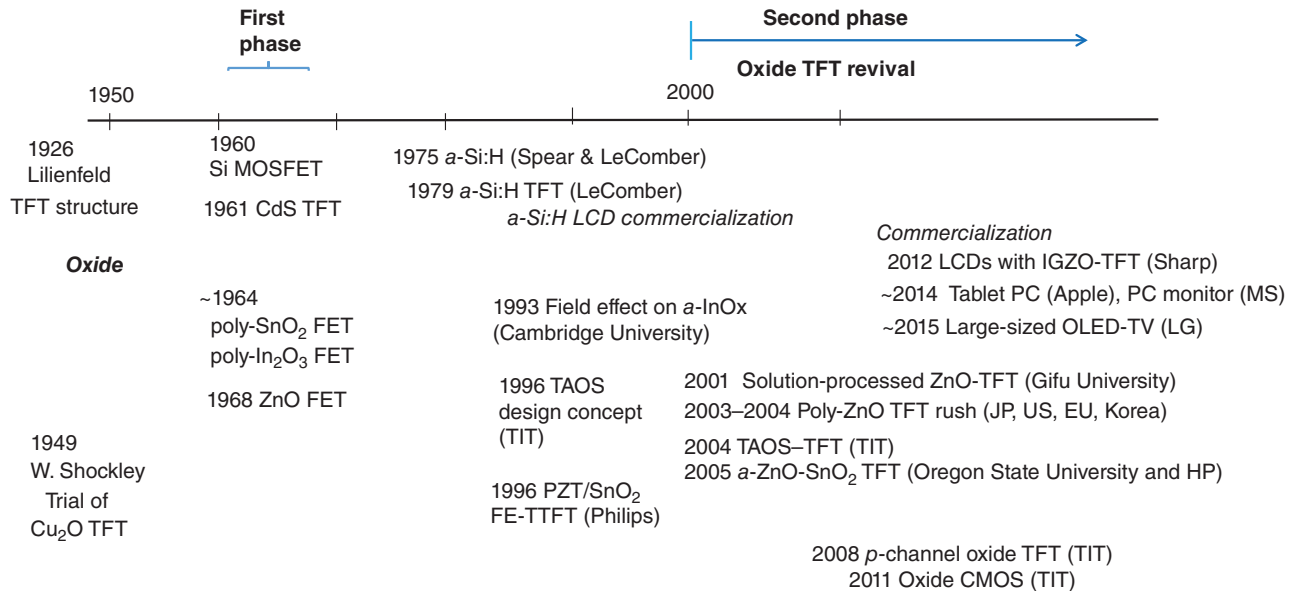


Figure 1.1.3 History of oxide TFTs and relevant technology.

on current modulation in the thin films SnO_2 , In_2O_3 , and ZnO, representative transparent oxide conductors, were reported, but papers on these oxide TFTs almost disappeared from open domains until circa 2000. Research on ZnO-TFTs was revisited extensively by many groups. Among them is a noteworthy paper in 2001 by Ohya et al., who reported on ZnO-TFTs that were prepared by solution process (i.e., drop-coating of $\text{Zn}(\text{CH}_3\text{COO})_2$ solution and subsequent heating in air) [1]. This is the first report on oxide TFTs fabricated by nonvacuum processes. Since oxide semiconductors are chemically stable in an ambient atmosphere at elevated temperature, unlike conventional semiconductors, this approach utilizing this intrinsic nature of material became a milestone in the fabrication of solution-derived oxide TFTs, which is now an active subject. Many papers on ZnO-TFTs deposited by sputtering or pulsed-laser deposition were reported [2], but serious issues—such as poor reproducibility and large hysteresis, arising mainly from the complex grain-boundary nature—were pointed out.

A design concept and several examples of TAOSs with large electron mobility were proposed in 1996 [3]. As for TFTs with amorphous oxides, in 1993 Adkins et al. examined field modulation on amorphous InO_x and reported a current on/off ratio of 2–3 [4]. Such a small on/off ratio comes from high carrier concentration. Suppression and carrier concentrations and stabilization of a low carrier state in *a*- InO_x are still challenging even now. Good-performance AOS-TFTs were reported for IGZO [5] in 2004 and ZnSnO_x [6] in 2005. Since then, a variety of AOS-TFTs have been reported to date [7].

In contrast to *n*-channel AOS-TFTs, the progress in *p*-channel has been much slower, and no satisfactory devices have been realized to date. Although a series of *p*-type transparent oxide semiconductors have been reported since 1997 [8], none of them works as a good TFT channel like Cu_2O . The formation of high-density surface defects arising from oxidation of Cu^+ is likely responsible for this. *P*-channel oxide TFTs were first realized in SnO [9] in 2008, and all complementary metal-oxide semiconductors (CMOSs) were reported [10] in 2011 utilizing the ambipolar nature of SnO. The performance of SnO-TFTs is still insufficient for practical application [11]. As for amorphous *p*-channel TFTs, very few have been reported [12] as far as the author knows. An amorphous oxide *p*-*n* junction using *p*- ZnRhO_x /*n*-IGZO exhibiting clear rectifying characteristics was reported [13] in 2003, but amorphous ZnRhO_x did not work as a *p*-channel TFT like *a*-vanadium-based oxides. High midgap state density arising from a *d* orbital would hinder the smooth E_F shift by gating.

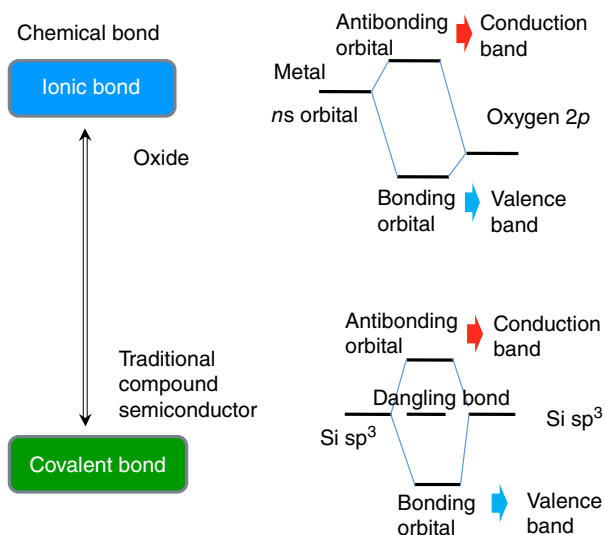


Figure 1.1.4 Comparison in chemical bonding and band formation between oxide and Si.

1.1.3 Oxide and Silicon

Oxide semiconductors made of typical metals are, in general, *n*-types except for several materials. This is a natural consequence of the chemical-bonding nature of oxides. Figure 1.1.4 shows schematic energy diagrams of ionic oxides and silicon. In ionic oxides, the nature of the CBM, which works as an electron pathway, totally differs from that of the VBM, which works as a hole pathway. The CBM in ionic oxides is primarily composed of unoccupied *s* orbitals of cations, and the contribution of oxygen 2*p* orbitals is limited. The spatial spread of this unoccupied *s* orbital is so large that direct overlap between the *s* orbitals of the neighboring cations is possible in PTM oxides; therefore, an effective mass of electrons is small in these oxides. In fact, some ionic oxides satisfy such situations with large electron mobilities of up to $\sim 100 \text{ cm}^2(\text{Vs})^{-1}$ and are called transparent conductive oxides (TCOs) represented by In_2O_3 , SnO_2 , ZnO , and Ga_2O_3 . *N*-type material can be realized with a proper choice of metal cation, but *p*-type material is difficult because oxygen 2*p* orbitals are generally localized at the VBM.

1.1.4 Transparent Amorphous Oxide Semiconductors

1.1.4.1 Electronic Structures

What happens if these TCO materials become an amorphous state? In an amorphous state, structural disorder concentrates on an energetically weak structural unit. In most amorphous materials, structural disorder appears prominently as the bond-angle distribution. When the bond angle has a large distribution, how is the effective mass (i.e., the transfer rate between neighboring cation *s* orbitals or overlap integrals) modified for carrier electrons? We considered the two cases: (i) covalent semiconductors and (ii) ionic semiconductors. In the former case, the magnitude of the overlap between the unoccupied orbitals of the neighboring atoms is very sensitive to the variation in bond angle. As a consequence, rather deep localized states would be created at somewhat high concentrations; thereby, the drift mobility would be largely degraded.

On the other hand, the magnitude of the overlap in the latter case is critically different depending on the choice of metal cations; when the spatial spread of the *s* orbital is larger than the inter-cation distance, the magnitude should be insensitive to the bond-angle distribution because the *s* orbitals are isotropic in shape. As a consequence, we may anticipate that these ionic amorphous materials have large electron mobility comparable to that

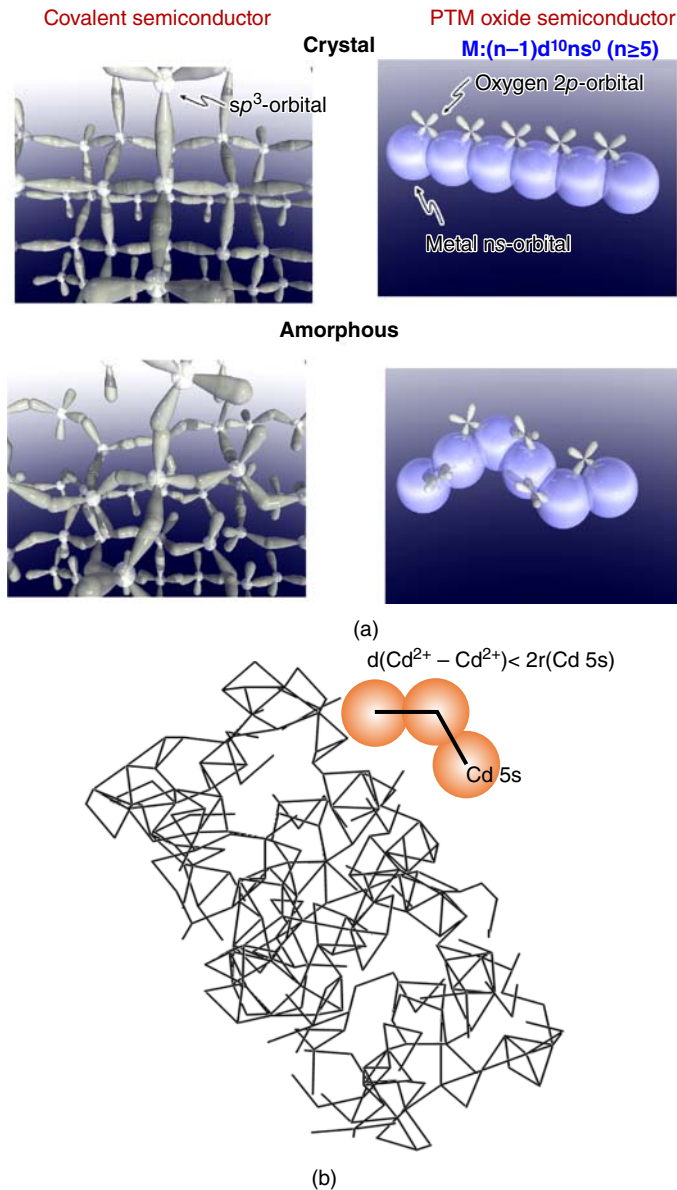


Figure 1.1.5 (a) Comparison in orbital constitution at the conduction band minimum (CBM) between covalent-type semiconductors and post transition metal oxide semiconductors, and (b) a percolated conduction network at the conduction band bottom of amorphous $2CdO \cdot GeO_2$.

in the corresponding crystalline phase. In the case that the spatial spread of the metal s orbital is small, such a favorable situation cannot be expected [3, 12]. The spatial spread of the s orbital of a metal cation is primarily determined by the principal quantum number (n) and is modified by the charge state of the cation, as discussed for the crystalline TCOs. Thus, candidates for high-mobility TAOSs are found in oxides of PTM cations with an electronic configuration of $(n-1)d^{10}ns^0$, where $n \geq 5$ [3, 12] (for crystalline oxide semiconductors, this requirement is relaxed to $n \geq 4$, as exemplified by ZnO with the $(3d)^{10}(4s)^0$ configuration). Figure 1.1.5a shows the difference in orbitals between Si and a PTM oxide and between crystalline and amorphous states. The drastic reduction of the electron mobility in the amorphous state from c-Si may be understood intuitively from that figure, whereas

mobility in c-PTM oxides is reserved even in the amorphous state. In a sense, the situation of the CBM in PTM oxides is similar to that in amorphous metal alloys (conductivity is slightly lower than that in crystalline alloys), because metal orbitals dominantly constitute the electron pathways. This simple idea is demonstrated quantitatively by observing the DOS by inverse photoelectron spectroscopy and analyzing the computed DOS on atomic positions determined by a combination of X-ray radial distribution function with reverse Monte Carlo simulation. Figure 1.1.5b illustrates the connectivity of Cd 5s orbitals at the CBM of amorphous 2CdO-GeO₂ as an example of TAOS. Here, Cd²⁺ with (4d)¹⁰(5s)⁰ meets the requirement for a PTM cation. Here, two Cd²⁺ ions were connected by a line for visualization of orbital overlap when a 2×Cd 5s orbital radius (Slater) is larger than the interatomic separation. It is clearly observed that the lines are 3D-connected throughout the sample, forming a percolated electron pathway [12].

1.1.4.2 Materials

Due to the requirements discussed in this chapter for high-mobility oxides, major TAOS materials need to contain In³⁺ or Sn⁴⁺, each of which have a (4d)¹⁰(5s)⁰ configuration, and its amount is required to be beyond the percolation threshold of its 5s orbitals at the CBM. There is a distinct difference between In and Sn in oxide materials. The valence state of In is stable at +3, while Sn takes two charge states, +4 and +2, depending on its environment. Since the filled 5s states are located at above VBM, Sn²⁺ with a 5s² configuration does not work, unlike Sn⁴⁺. TAOS materials with many different compositions have been reported to date, and the materials that work as excellent TFT channels are almost restricted to In- and/or Sn-containing systems.

Here, a-In-Ga-Zn-O (a-IGZO) [3, 14] is taken as a representative TAOS material. In a-IGZO, the In³⁺ ions contribute to a large electron mobility, and thus are called “mobility enhancers.” Ga with larger ionic strength (ionic charge/ionic radius) forms a stronger chemical bond with oxygen and suppresses the formation of oxygen deficiency and the generation of conduction electrons, and thus it is called a “stabilizer” or “suppressor.” The role of Zn taking tetrahedral coordination is not clear but is expected to stabilize amorphous structure; this is known in glass science as a “network former.” Therefore, increasing the In content increases the electron mobility but also increases residual electron density and tends to cause negative threshold voltage (V_{th}) in TFTs. Addition of a suppressor like Ga reduces the electron density (N_e) if the same deposition condition is employed, but it decreases the electron mobility. The decrease in mobility is caused by two factors: (i) reduction of the In content and (ii) reduction of electron mobility due to the small N_e , as will be explained further in this chapter. Pure In₂O₃ and ZnO do not form stable amorphous structures, even if deposited at room temperature (RT) without substrate heating. Mixing of two or more metal cations is thus necessary to stabilize the amorphous structure. TAOS materials for TFT channels are made from a combination of mobility enhancers and suppressors. The first material is a-IGZO with the nominal atomic ratio of In:Ga:Zn = 1:1:1 (called “111” composition), and also another composition of In:Ga:Zn = 2:2:1 (“221” composition) has been examined. Oregon State University (OSU) and the HP group [6] proposed Zn-Sn-O (ZTO) and Zn-In-O (ZIO) TFTs just after the first report of a-IGZO TFTs, which exhibited high $\mu_{TFT} > 50 \text{ cm}^2/(\text{Vs})$ by annealing at 600 °C. A variety of combinations have been reported for TAOS-TFTs. TAOS materials containing In³⁺ and Sn⁴⁺ were also reported as ITZO (In-Sn-Zn-O). The advantages of ITZO TFTs are high ($\mu_{TFT} > 30 \text{ cm}^2/(\text{Vs})^{-1}$), and they have good robustness and selectivity against wet etching for backchannel etched TFTs. In contrast, ITZO requires high oxygen partial pressure during sputtering to suppress the electron density so as to fit to normally off TFTs, but the high P_{O₂} condition deteriorates the deposition rate seriously. It is proposed that the addition of water to the sputtering atmosphere improves this issue.

TFT mobility and stability are in a trade-off relationship in many cases. A typical example is a-IZO (ZnO content 10%) material. The amorphous structure of In₂O₃ is much stabilized by the incorporation of ZnO, and μ_{Hall} does not degrade. Conventionally sputtered thin films of this TAOS material are used as amorphous TCOs (transparent metal), not semiconductors. When IZO is sputtered in highly oxidizing conditions, the thin films with low enough

N_e to use as a TFT channel layer can be fabricated. TFTs based on such a thin film exhibit high μ_{FE} , such as $50 \text{ cm}^2/(\text{Vs})$, and the off-current continuously increases with time and eventually loses device performance.

1.1.4.3 Characteristic Carrier Transport Properties

TAOS has several common and unique properties that are not seen in conventional amorphous semiconductors [14]. First are their large electron mobilities $> 10 \text{ cm}^2/(\text{Vs})^{-1}$, which are higher by 1–2 orders of magnitude than those in a-Si:H. Second is that a degenerate state can be realized. This is totally different from the other amorphous semiconductors. For instance, c-Si is easily changed to the degenerate state by impurity doping ($\sim 10^{16} \text{ cm}^{-3}$), but no such state is attained in a-Si:H. That is, carrier conduction takes place by hopping through localized tail states in conventional amorphous semiconductors. This is the reason why mobility in the amorphous state is so small compared with that in the crystalline state. On the other hand, in TAOS, the E_F can exceed the mobility gap easily by carrier doping, leading to band conduction. It is considered that this striking difference originates from that in the chemical-bonding nature between the materials (i.e., strong ionic bonding with spherical potential is very favorable to forming a shallow tail state with a small DOS).

Hall effect measurements, which are a standard method in crystalline semiconductors, cannot be used for amorphous semiconductors. The reason is that the mean free path is so short, being comparable to or smaller than interatomic separation. On the contrary, TAOS materials give distinct Hall voltages, and the evaluated N_e and mobility of carriers are reliable because the mean free path is several nanometers, which is much larger than the interatomic separation. Carrier transport properties of a-IGZO are shown in Figure 1.1.6 as an example of TAOS. It is noted that mobility (μ_{Hall}) largely depends on N_e due to the presence of potential barriers arising from structural disorder. μ_{Hall} increases with increasing N_e and finally exceeds $10 \text{ cm}^2/(\text{Vs})^{-1}$ if N_e exceeds $\sim 10^{18} \text{ cm}^{-3}$. The activation energy of mobility is continuously decreased with N_e , and eventually the degenerate state is realized at $N_e = 10^{19} - 10^{20} \text{ cm}^{-3}$. This μ_{Hall} versus N_e behavior is explained by the percolation conduction model, in which

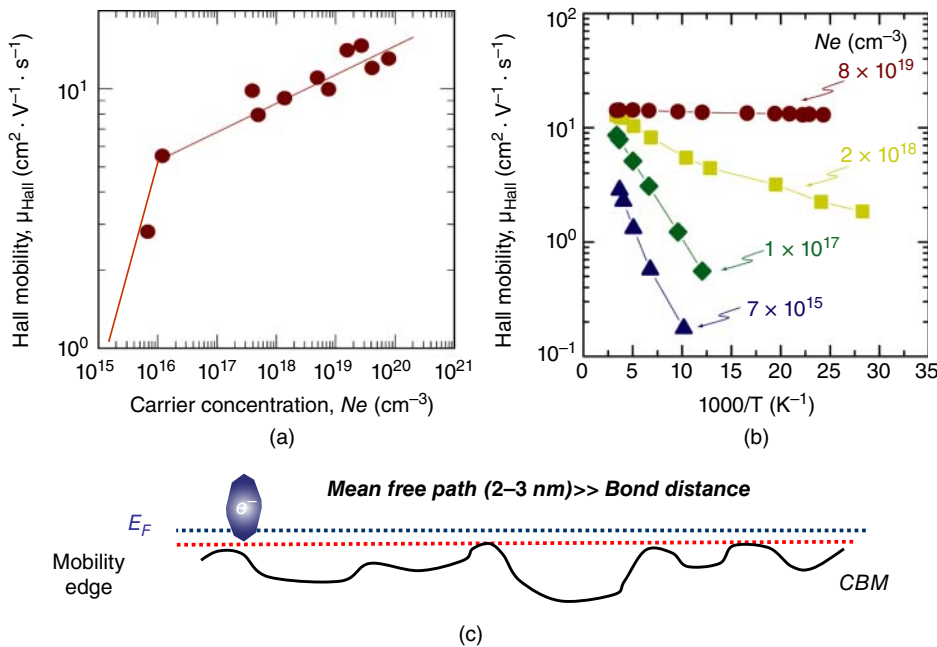


Figure 1.1.6 Electron transport (Hall mobility) in a-IGZO thin films and a schematic potential barrier at the CBM.

electron transport is controlled by distributed potential barriers above CBM (Figure 1.1.6c) [15–17]. If the TAOS is very defective or with very low N_e , hopping conduction would be dominant.

1.1.4.4 Electronic States

TFTs are devices in which source–drain current is modulated by applying a voltage to the gate insulator over several to ten orders of magnitude, as shown in Figure 1.1.7. Thus, both the density of in-gap state and the tail state are called subgap states hereafter; n -channel semiconductors are critical for TFT applications because these states work as carrier traps. The dominant factor of μ_{FE} is partly different from that of μ_{Hall} because μ_{FE} is expressed roughly by $\mu_{Hall} (N_{ind} - N_{trap}) / N_{ind}$, where N_{ind} is the total electron density induced by the gate voltage and N_{trap} is the density of the induced electrons trapped by subgap defects and tail states. Therefore, low N_{trap} is important to obtain high μ_{FE} , and the low N_{trap} is confirmed by TFT analyses, coefficient of variation (C-V) analyses, and so on, as shown in Figure 1.1.8. These studies have revealed that these localized state densities in TAOSs are

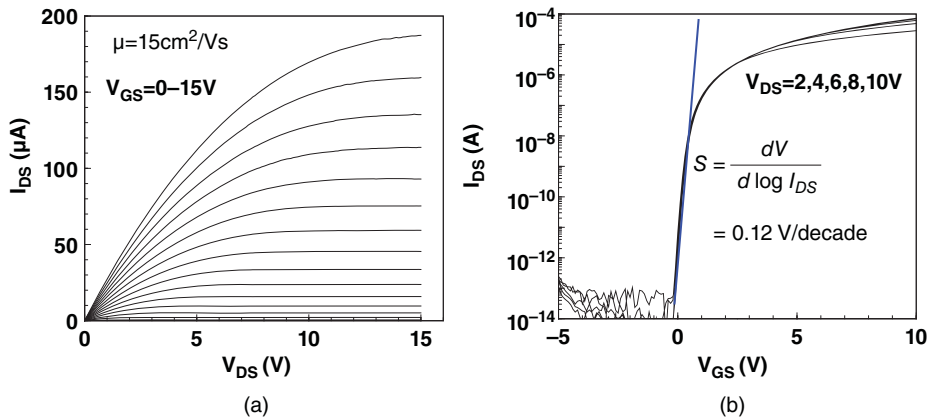


Figure 1.1.7 Typical a-IGZO-TFT characteristics. The thin film was deposited by sputtering using an IGZO (In:Ga:Zn=1:1:1) target. The device size is 30 μm (W), 50 μm (L), and 40 nm (thick). Gate insulator: thermal SiO_2 (150 nm) on Si. Contact: Ti/Au. The device was post-annealed at 300 $^\circ\text{C}$ for 1 h in ambient atmosphere before contact formation.

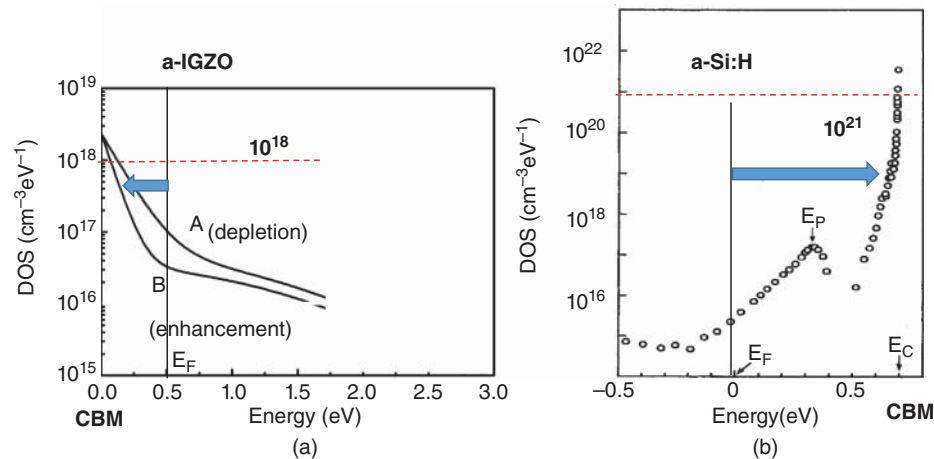


Figure 1.1.8 Tail state density in a-IGZO and a-Si:H. The former was evaluated from a simulation of TFT characteristics. The latter was taken from Ref. [40]. An arrow indicates the Fermi level shift to induce band conduction at the CBM.

2–3 orders of magnitude smaller than that of a-Si:H where E_F is close to CBM. This striking difference is the main reason why the band conduction can be induced in TAOS but not in a-Si:H by biasing gate voltage. (Bob Street [18] successfully explained why E_F cannot exceed the mobility gap.) The low N_{trap} is explained also by the electronic structure specific to the high ionicity of TAOS; that is, since Coulombic potential is independent on angle, the energy level is very insensitive to the variation in bond angle, which is the dominant randomness in amorphous materials, compared with the potential in a covalent bond. Thus, tail state density in TAOS is much lower than that in a-Si:H.

Figure 1.1.9 illustrates these electronic structures of a-IGZO [14]. Noteworthy is the presence of a large DOS ($10^{19-20} \text{cm}^{-3}$) above the VBM. This DOS was first observed [19] for thin films by hard X-ray photoemission spectroscopy (HAX-PES) using a synchrotron radiation facility (6–8 keV). HAX-PES has two advantages over conventional lab-PES; the first is to be bulk sensitive originating from the large escape depth of the photoelectron. This makes it possible to get reliable information from as-prepared thin films without any surface treatment such as sputtering. The other is large ionization cross-section for s -state electrons, which are associated with oxygen vacancy, hydrogen anions, and low valence cations with ns^2 electron configurations such as In^+ and Ga^+ . Since this DOS is located above the VBM and far below the E_F , an n -channel TFT operation does not suffer from their influence, fortunately. However, this DOS plays a critical role in energy saving of the devices and TFT degradation under the dominant operation mode (negative bias under illumination stress [NBIS]), which is called NBIS instability. The E_F cannot push down under negative gate voltage due to the presence of this large DOS (i.e., the p -channel does not open when negative bias is applied). This feature makes a contrast with a-Si:H TFTs, which show ambipolar operation (i.e., the drain current is increased when negative bias is further applied to the gate). Since TFTs for LCDs dominantly stay in an off-state, the unipolarity of TAOS-TFTs leads to energy saving. This is the reason why low off-currents of IGZO-TFTs are much lower than those of a-Si:H and low-temperature processed polysilicon (LTPS)-TFTs.

This large DOS above the VBM works as the source of NBIS instability, which is induced by subgap light illumination under negative bias. The electron in the DOS is excited to the CBM by subgap illumination. The electron

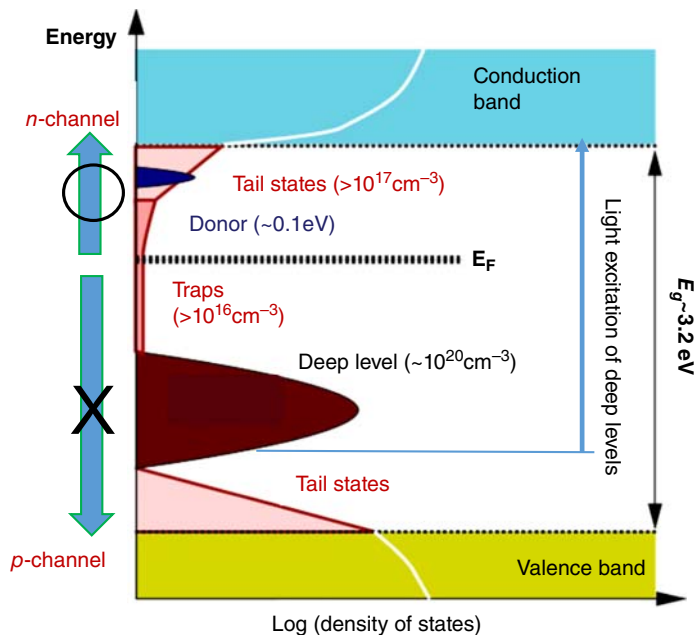


Figure 1.1.9 An experimentally clarified electronic structure of a-IGZO and TFT operation.

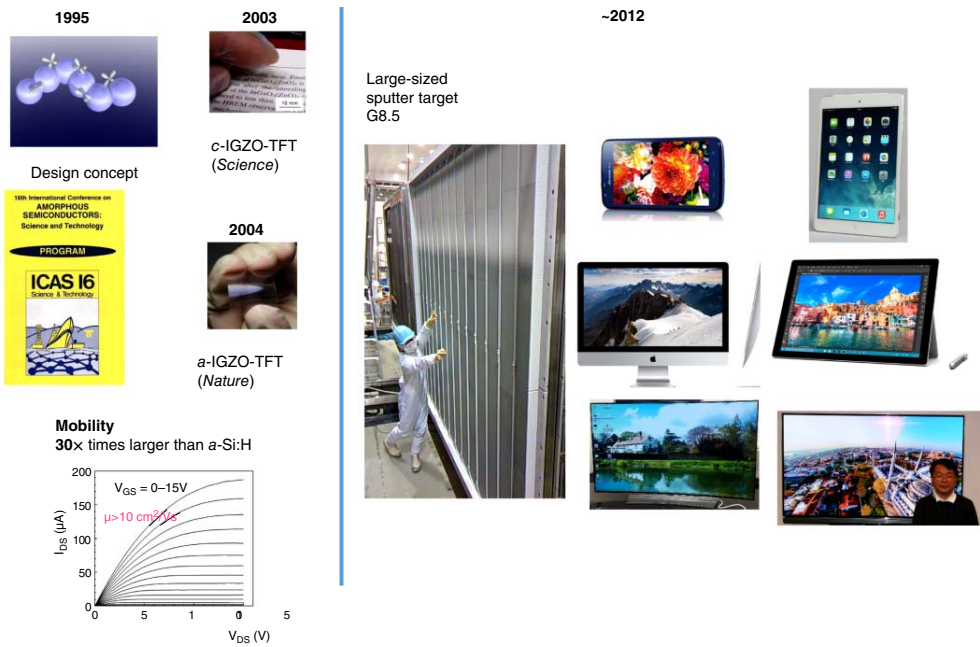


Figure 1.1.10 Progress in IGZO-TFTs and their display applications.

excited to the CBM is easily diffused away due to the high electron mobility at the CBM, while the remaining hole drifts to the interface between the channel and the gate insulator and is trapped there to form a fixed positive charge. As a result, the threshold voltage shifts to the negative voltage side. NBIS instability [20] was first reported in polycrystalline ZnO-TFTs and was found in almost all of the *n*-type oxide TFTs, irrespective of whether they were crystalline or amorphous. This suppression is an important issue for practical application of oxide-TFTs for displays because the threshold voltage shifts result in output current changes, in particular for OLEDs, which are driven by current.

Figure 1.1.10 summarizes the progress of IGZO-TFTs and their application to the backplanes of flat-panel displays in smartphones, tablet PCs, PC monitors, and OLED-TVs period. The first reported IGZO-TFTs were based on epitaxial thin films, and their mobility was $\sim 80 \text{ cm}^2/(\text{Vs})$ [21], which is comparable to that of poly-Si TFTs. Amorphous IGZO-TFTs fabricated on plastic substrates were published in 2004, and the mobility was $\sim 10 \text{ cm}^2/(\text{Vs})$ [5]. It is obvious from Section 1.1.4.2 that the ratio of Ga to In controls the mobility and stability. A higher In fraction enhances mobility while reducing the stability. A key reason why IGZO-TFTs are widely applied to displays is that since this composition forms a stable crystalline phase, large-sized and dense ceramics can be obtained easily for sputtering targets [22]. Large-sized OLED-TVs are driven by a-IGZO-TFTs. Two major features of a-IGZO-TFTs, high mobility and excellent homogeneity over a large size, are fully utilized in these products.

1.1.5 P-Type Oxide Semiconductors for Display Applications

N-Type transparent oxide semiconductors can be designed by selecting metal cations with spatially spread *s* orbitals that constitute the CBM and a crystalline structure with a smaller separation between metal cations, as illustrated in Figure 1.1.11a. However, no guidelines for designing *p*-type semiconductors were presented until 1997 [8]. Needless to say, *p-n* junctions are the origin of various semiconductor functions; therefore, high-quality *p*-type transparent semiconductors are essential for not only transparent oxide electronics but also all-solid dye-sensitized solar cells. For wide-gap oxides, the VBM, which serves as the conduction path of holes, is mainly composed of oxygen *2p* orbitals, and the contribution of the orbitals of metal cations is generally small. Therefore, the VBM is little dispersed (i.e., the effective mass of holes is large), and the energy level is deep to dope holes. This is why *p*-type transparent oxide semiconductors are difficult to realize. Resolving this problem is a key strategy in realizing *p*-type transparent oxide semiconductors. Three previously proposed approaches are given in this section.

1.1.5.1 Oxides of Transition Metal Cations with an Electronic Configuration of $(n-1)d^{10}ns^0$ ($n = 4$ or 5)

Although transition metal cations have orbitals with energy levels close to those of oxygen *2p* orbitals, most of them absorb visible light owing to a *d-d* transition [23]. Therefore, oxides of cations with closed-shell *d* orbitals, such as Cu^+ and Ag^+ , are considered to have the potential to exhibit *p*-type conductivity. As shown in Figure 1.1.11b, for such oxides, the antibonding orbital component of the bond composed of metal *d* orbitals and oxygen *2p* orbitals constitutes the VBM, and the holes doped into the VBM are delocalized to realize *p*-type conductivity. A typical example is delafossite CuMO_2 ($M = \text{Al}^{3+}$, Ga^{3+} , and In^{3+}) with dumbbell-type O–Cu–O bonds as the building block. Although several *p*-type transparent semiconductors have been found to date, no good TFT operation based on Cu^+ has been reported to date like the Cu_2O case by Shockley. The high concentration of hole traps at the surface associated with oxidation of Cu^+ would be the most plausible cause of these results.

1.1.5.2 Oxides of Metal Cations with an Electronic Configuration of ns^2

Cations with an electronic configuration of ns^2 have lone pairs similar to those of anions [9]. For the oxides of such metal cations, the VBM is mostly occupied by *s* orbitals, as shown in Figure 1.1.11c. Lone pairs occupy the

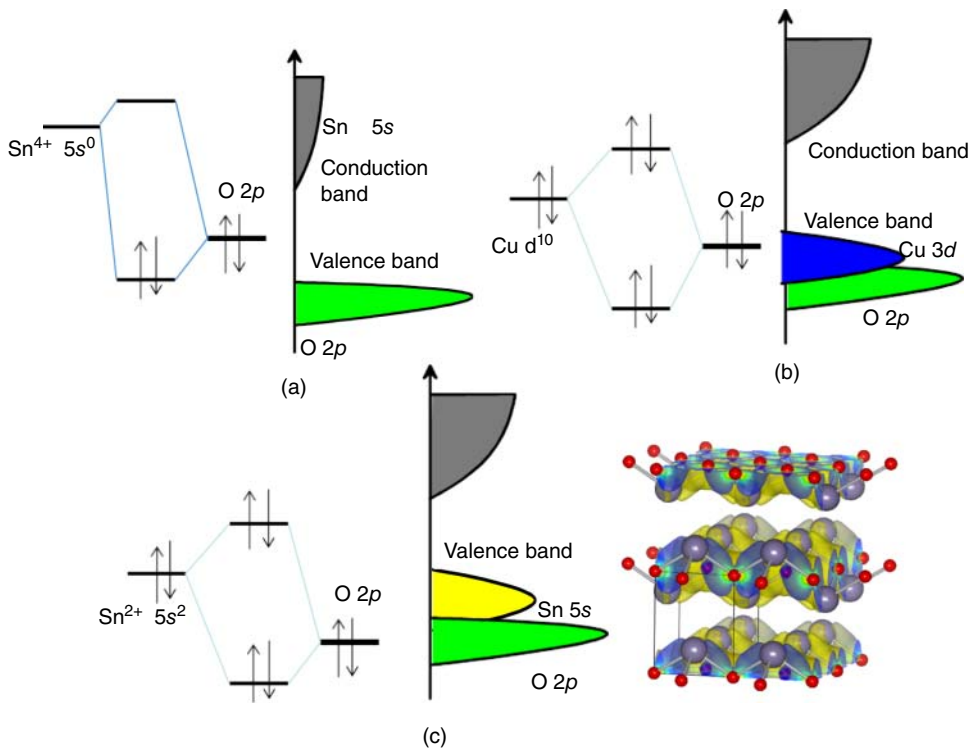


Figure 1.1.11 Schematic energy diagram: (a) *n*-type SnO_2 , (b) *p*-type Cu_2O , and (c) *p*-type SnO . The right is an orbital drawing of the VBM. Sn 5s electrons with large spread occupy the VBM.

spatially dispersed *s* orbitals, which overlap with the *s* orbitals of adjacent cations via the oxygen, forming a largely dispersed band above the oxygen 2*p* band. Oxides of Sn^{2+} with an electronic configuration of $5s^2$ are typical and exhibit *p*-type conductivity in Hall effect measurements. In addition, the first-ever oxide TFT that can operate as a *p*-channel TFT was realized using SnO for the active layers [9].

The realization of CMOS based on an oxide semiconductor was a long-standing issue in oxide electronics. This objective was first attained in 2011 using SnO [9]. Although much improvement has been reported [11, 24], the CMOS performance is still insufficient for applications. Low-temperature processing as well as improvement of mobility are strongly required for display applications.

It has been reported that chalcogenides and oxides of Pb^{2+} and Bi^{3+} , both with an electronic configuration of $6s^2$, cannot be used to enhance hole transport properties because the energy level of 6*s* electrons is much deeper than that of the VBM. Although oxides of Sb^{3+} with an electronic configuration of $5s^2$, similar to that of Sn^{2+} , are expected to exhibit *p*-type conductivity, no examples of such oxides have been reported to date.

1.1.5.3 Oxides of Metal Cations with an Electronic Configuration of nd^6

For oxides of Rh^{3+} and Ir^{3+} , both with an electronic configuration of $4d^6$ or $5d^6$, these cations stabilize in the low-spin-state octahedral configuration, where electrons occupy the three orbitals d_{xy} , d_{yz} , and d_{zx} [25]. *4d* and *5d* orbitals are spatially spread, and the state in which two electrons occupy each of the three *d* orbitals is similar to that in Section 1.1.5.2, that is, a pseudo *s* orbital with a large spread. When doped with holes, these oxides are expected to exhibit *p*-type conductivity. A typical example is ZnRh_2O_4 , which has a normal spinel structure [25]. Similar to the case of ZnO , the Zn^{2+} ions in this material are coordinated in tetrahedra, which are not continuously connected

and do not exhibit *n*-type conductivity. ZnRh_2O_4 is the only oxide that is known to exhibit *p*-type conductivity even in the amorphous state, and it has been reported to form *p-n* diodes on plastic substrates [26] when combined with TAOS. Subsequently, *p*-type conductivity was reported for ZnCo_2O_4 as an extension of this series to the $3d^6$ system.

These materials work as *p*-type semiconductors for the *p-n*-junction but not as *p*-channel material in TFTs because of the high concentrations of vacant *d* levels, which serve as hole trapping in the band gap.

1.1.6 Novel Amorphous Oxide Semiconductors

Recently, two novel-type AOSs toward display applications were reported based on rather different design concepts: an amorphous electride (a-C12A7:e⁻) and amorphous ZnO-SiO₂ (a-ZSO).

Electrides are materials in which electrons serve as anions [27]. This conceptionally novel material was first synthesized in organic crystals. Although these attracted attention as an exotic material, almost no information had been obtained on the physical properties because they are extremely sensitive to heat, O₂, and H₂O.

In 2003, an inorganic electride material derived from 12CaO·7Al₂O₃ crystal (C12A7) was reported [28]. C12A7 is a wide-gap insulator composed of densely packed, subnanometer-sized cages with a positive charge, and it is thermally stable with a melting point of 1415 °C. The unit cell includes two molecules and 12 cages that have a free inner space of ~0.4 nm in diameter and can be represented as $[\text{Ca}_{24}\text{Al}_{28}\text{O}_{64}]^{4+} + 2\text{O}^{2-}$. The former denotes the cage framework, and the latter is called “free oxygen ions” that compensate for the positive charge of the framework. These oxygen ions are loosely bound to the cages because the cage diameter is ~50% larger than the O²⁻ size (0.28 nm). They succeeded in extracting this free O²⁻ ion, regarded as the counter anion to the giant framework cation, by a chemical reduction method and injected electrons instead. Since the resulting material (hereafter, C12A7:e⁻) with the composition of $[\text{Ca}_{24}\text{Al}_{28}\text{O}_{64}]^{4+} \cdot (4e^-)$ may be regarded as electride, this material became the first RT-stable electride.

Amorphous C12A7:e⁻ thin films were successfully fabricated by conventional sputtering of a C12A7:e⁻ ceramic target in O₂-free atmosphere, and the resulting thin films contain a high anionic electron concentration comparable to that in crystalline C12A7:e⁻ [29]. Anionic electrons exist in subnanometer-sized space coordinated by 2 Al³⁺ or a Ca²⁺ and an Al³⁺. The work function of a-C12A7:e⁻ is ~3.0 eV, which is larger than that of c-C12A7:e⁻ (2.4 eV) but still rather lower than that of conventional transparent oxide semiconductors (comparable to metal Ca), and it is chemically inert and optically transparent as shown in Figure 1.1.12. There are two types of OLEDs with different stacking, normal type (cathode top) and inverted type (cathode bottom). An inverted type is better than a normal one, as the device structure emitting light can radiate upward through a cathode of transparent electrode (indium tin oxide [ITO]). However, the fabrication of an inverted structure was practically hard due to the lack of an appropriate electron injection layer (EIL) because a combination of LiF and Al does not work for this structure (deposition sequence Al followed by LiF). An inverted structure of OLEDs with comparable performance to a normal structure was realized by using a-C12A7:e⁻ with a low work function and high optical transparency as the EIL.

Second is a-ZSO, ZnO-SiO₂. A ZSO thin film has a low work function (~3.5 eV), which is lower by ~1 eV than ZnO and also enables relatively higher mobility (0.3–1.0 cm²/(Vs)) than those of the *n*-type organic semiconductors [30]. In addition to high visible transparency and good chemical stability, a-ZSO can form ohmic contact with various metals irrespective of the work function of partner metals. These properties almost completely meet the requirements to be electron injection/transport layers in OLEDs and perovskite LEDs. The effectiveness of this semiconductor was demonstrated by the realization of high-performance perovskite LEDs [31], as shown in Figure 1.1.13, and efficient tandem OLEDs [32]. These exceptional properties originate from a characteristic nanostructure composed of ZnO nanocrystals separated by thin amorphous zinc silicate layers with larger ionization potential and smaller electron affinity than ZnO. This nanostructure makes it possible to confine wave function in ZnO nanocrystals, which in turn widens the band gap due to the quantum size effect. Since E_F is

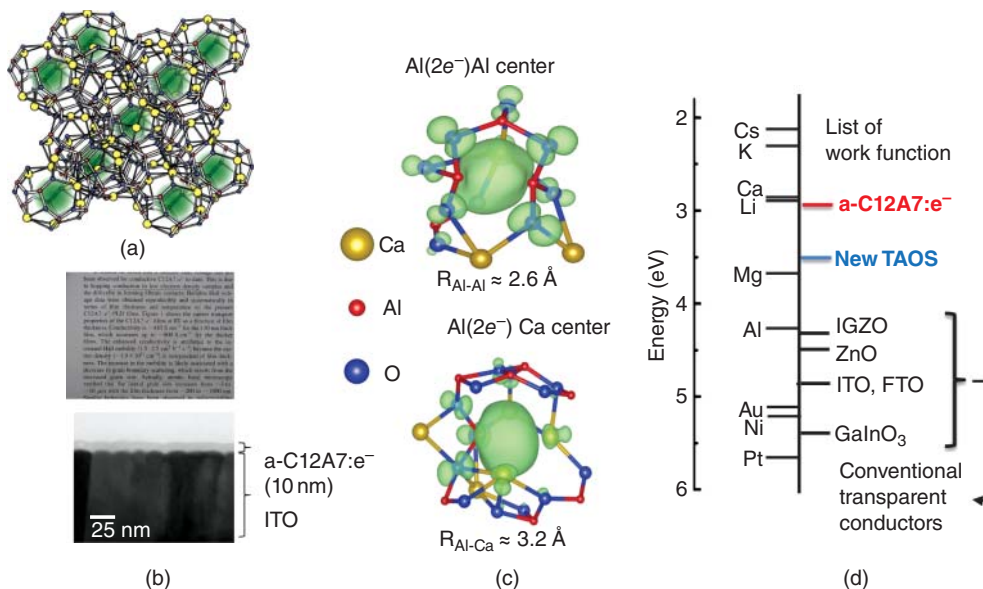


Figure 1.1.12 C12A7 electride. (a) c-C12A7:e⁻, (b) photos of sputter-deposited a-C12A7:e⁻, (c) two anionic electron sites in a-C12A7:e⁻, and (d) the work function of C12A7:e⁻ and relevant materials.

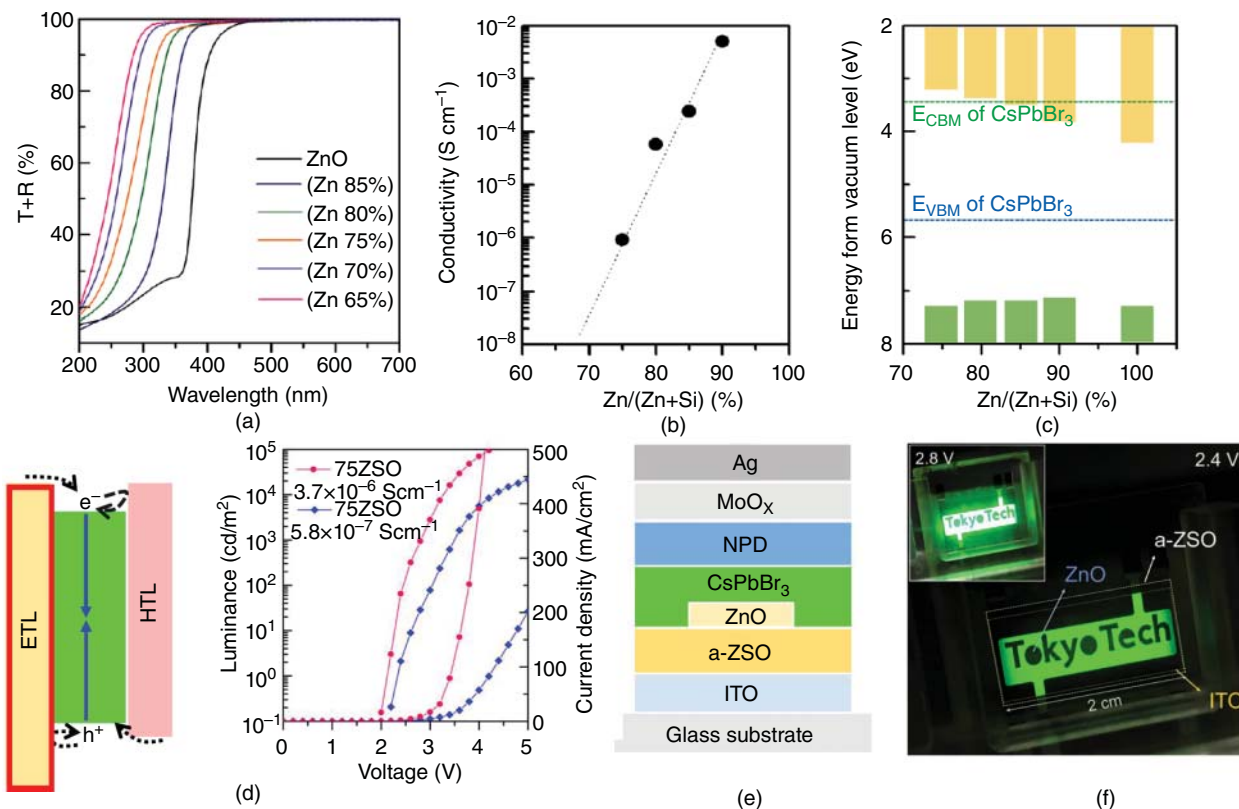


Figure 1.1.13 Amorphous ZnO-SiO₂. (a) Optical absorption of 200-nm-thick thin films, (b) conductivity at RT, and (c) variation in the band-edge position with composition. The band-edge positions of green emitting layer CsPbBr₃ are also indicated. (d–f) EL device structure and EL characteristics. It is visually evident that a-ZSO works much better than ZnO. Note that the emission intensity goes up to 50,000 cd/cm² at 5 V.

located at the CBM, this wide gap widening results in lower work function. ZnO nanocrystals in the material are conducting, due probably to the incorporation of Si to the Zn site, and they are not continuously connected by a thin insulating zinc silicate layer. Thus, mobility observed by hopping conduction through localized levels in the insulating zinc silicate layer is amply large compared with that of organic semiconductors used as the electron transport layer. This X-ray AOS is a kind of nanocomposite material utilizing the optical confinement effect of ZnO nanocrystals and electrically connected conducting ZnO nanocrystals connected by hopping conduction via a thin insulating ZnO-SiO₂ layer.

1.1.7 Summary and Outlook

This chapter outlines the background, fundamental understanding, and recent progress of AOSs for display applications in comparison with crystalline oxide semiconductors and amorphous silicon. An emphasis was placed on the electron transport and electronic structure of TAOSs represented by a-IGZO. Throughout this chapter, the author described design concepts based on a simple consideration of chemical bonding. The tremendous success of Si-based semiconductors has created splendid science and technology. Oxide semiconductors have a longer history than silicon semiconductors, but this had not led to practical device applications. IGZO-TFTs would be the first visible device application of oxide semiconductors. High-mobility TFTs using amorphous semiconductors are based on the intrinsic nature of *p*-block metal cation-based transparent oxides. Crystalline Si cannot meet the requirements for display technology, which needs large-sized thin films. Transparent amorphous oxide semiconductors have huge potential as backplane transistors for high-precision and energy-saving large-sized LCD panels. Application to electron transport/injection layers, which is hard to overcome with the existing technology, may be expected by developing new oxide semiconductors. Oxide is only one semiconductor material that is stable in air at high temperature. Thus, fabricating oxide semiconductors derived from solution is a process allowed for only oxide material. Although the resulting devices are still insufficient in stability and performance, further technical progress would lead to new applications. Review articles [23, 24] are helpful to compensate for the lack of this discussion in the present chapter.

Finally, the author would like to raise two technical challenges in transparent amorphous semiconductors:

1. *High-mobility p-channel TFTs*: Oxides are unfavorable as *p*-type semiconductors. The deep energy level and highly localized nature of O *2p* dominating the VBM make it hard to have high-mobility *p*-type conduction. Recently, transparent amorphous semiconductors with high mobility (~ 10 cm²/Vs) were reported in the Cu-Sn-I system [33]. As shown in Figure 1.1.14, filled I *5p* orbitals constituting the VBM with Cu *3d* orbitals may be regarded as the vacant *s* orbital of PTM cations in *n*-type TAOSs. The hole concentration in these materials is too high to operate as TFTs with enough current on/off ratio. Reduction of carrier concentration without degrading mobility is the current issue. If this issue could be overcome, good-performance transparent CMOS devices are possible with a combination with *n*-TAOS TFTs.
2. *High-mobility and high-stability TAOS-TFTs*: Amorphous IGZO-TFTs are now widely applied to flat-panel displays, replacing a-Si:H-TFTs. However, higher mobility TAOS-TFTs are demanded for circuit applications. It is well known that there is a phenomenological observation between mobility and stability (to various stresses) in oxide TFTs. Higher mobility TFTs are obtained in In-rich and/or In-Sn-based TAOSs such as InOx and In-Sn-Zn-O, but each of these TFTs is sensitive to stress (voltage, light, heat, and their combinations). Elucidation of the origin for this trade-off should give an effective clue to resolve the issue.

Materials science of TAOSs has greatly advanced in both fundamentals and device applications in the last two decades. A strong demand for new applications will be the engine to facilitate breadth in this area. There are several excellent review articles and monographs [34–39] on this subject, including those already cited in this chapter. The author encourages the reader to check these reviews if necessary. Very recently, a model from the trade-off described above was proposed and high mobility-highly stable *a*-ITZO TFTs were reported [41].

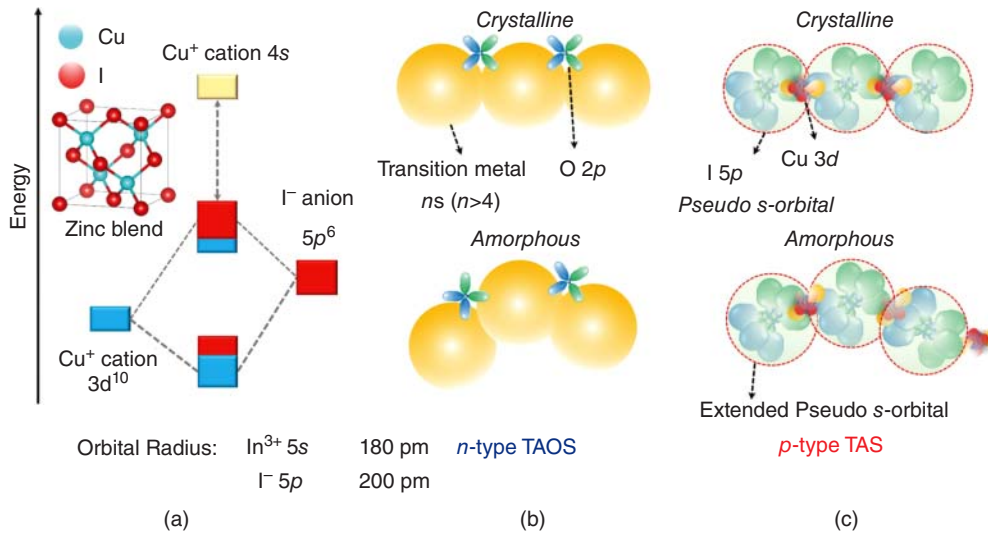


Figure 1.1.14 Amorphous Cu-Sn-I. (a) Crystal structure of γ -CuI zinc blends and schematic band structure. (b) Schematic orbital drawing of the CBM in crystalline and amorphous transparent conductive oxides (TCOs) based on a PTM cation with an electronic configuration $(n-1)d^{10}ns^0$, where $n > 4$. (c) Schematic orbital drawing of the VBM in CuI. Three $I 5p$ orbitals with a large spatial spread may be regarded as a pseudo s orbital similar to the $5s$ orbital with a large spread and a spherical shape.

References

- Ohya, Y., Niwa, T., Ban, T., and Takahashi, Y. (2001). Thin film transistor of ZnO fabricated by chemical solution deposition. *Japanese Journal of Applied Physics* 40 (1R): 297–298.
- Özgür, Ü., Hofstetter, D., and Morkoc, H. (2010). ZnO devices and applications: a review of current status and future prospects. *Proceedings of the IEEE* 98 (7): 1255–1268.
- Hosono, H., Kikuchi, N., Ueda, N., and Kawazoe, H. (1996). Working hypothesis to explore novel wide band gap electrically conducting amorphous oxides and examples. *Journal of Non-Crystalline Solids* 198: 165–169.
- Adkins, C.I., Hussain, T., and Ahmad, N. (1993). Field-effect measurements of carrier mobilities in transparent conducting films of amorphous indium oxide. *Journal of Physics: Condensed Matter* 5 (36): 6647.
- Nomura, K., Ohta, H., Takagi, A. et al. (2004). Room-temperature fabrication of transparent flexible thin-film transistors using amorphous oxide semiconductors. *Nature* 432 (7016): 488.
- Chiang, H.Q., Wager, J.F., Hoffman, R.L. et al. (2005). High mobility transparent thin-film transistors with amorphous zinc tin oxide channel layer. *Applied Physics Letters* 86 (1): 013503.
- Wager, J.F., Keszler, D.A., and Presley, R.E. (2008). *Devices in Transparent Electronics*, 83–151. Boston: Springer MA. This monograph portrayed research on oxide electronics at the initial stage of oxide TFTs (up to 2006) along with the fundamentals of TFT physics.
- Kawazoe, H., Yasukawa, M., Hyodo, H. et al. (1997). P-type electrical conduction in transparent thin films of CuAlO_2 . *Nature* 389 (6654): 939–942.
- Ogo, Y., Hiramatsu, H., Nomura, K. et al. (2008). p -channel thin-film transistor using p -type oxide semiconductor SnO. *Applied Physics Letters* 93 (3): 032113.
- Nomura, K., Kamiya, T., and Hosono, H. (2011). Ambipolar oxide thin-film transistor. *Advanced Materials* 23 (30): 3431–3434.

- 11 Wang, Z., Nayak, P.K., Caraveo-Frescas, J.A., and Alshareef, H.N. (2016). Recent developments in *p*-type oxide semiconductor materials and devices. *Advanced Materials* 28 (20): 3831–3892.
- 12 Narushima, S., Orita, M., Hirano, M., and Hosono, H. (2002). Electronic structure and transport properties in the transparent amorphous oxide semiconductor $2\text{ CdO} \cdot \text{ GeO}_2$. *Physical Review B* 66 (3): 035203.
- 13 Narushima, S., Mizoguchi, H., Shimizu, K. et al. (2003). A *p*-type amorphous oxide semiconductor and room temperature fabrication of amorphous oxide *p*-*n* heterojunction diodes. *Advanced Materials* 15 (17): 1409–1413.
- 14 Kamiya, T., Nomura, K., and Hosono, H. (2010). Present status of amorphous In–Ga–Zn–O thin-film transistors. *Science and Technology of Advanced Materials* 11: 044305-1–044305-23.
- 15 Kamiya, T., Nomura, K., and Hosono, H. (2009). Electronic structures above mobility edges in crystalline and amorphous In–Ga–Zn–O: percolation conduction examined by analytical model. *Journal of Display Technology* 5 (12): 462–467.
- 16 Lee, S., Ghaffarzadeh, K., Nathan, A. et al. (2011). Trap-limited and percolation conduction mechanisms in amorphous oxide semiconductor thin film transistors. *Applied Physics Letters* 98 (20): 203508.
- 17 Nenashv, A.V., Oelerich, J.O., Greiner, S.H.M. et al. (2019). Percolation description of charge transport in amorphous oxide semiconductors. *Physical Review B* 100 (12): 125202.
- 18 Street, R.A. (1982). Doping and the Fermi energy in amorphous silicon. *Physical Review Letters* 49 (16): 1187.
- 19 Nomura, K., Kamiya, T., Ikenaga, E. et al. (2011). Depth analysis of subgap electronic states in amorphous oxide semiconductor, a-In–Ga–Zn–O, studied by hard x-ray photoelectron spectroscopy. *Journal of Applied Physics* 109 (7): 073726.
- 20 Jeong, J.K. (2013). Photo-bias instability of metal oxide thin film transistors for advanced active matrix displays. *Journal of Materials Research* 28 (16): 2071.
- 21 Nomura, K., Ohta, H., Ueda, K. et al. (2003). Thin-film transistor fabricated in single-crystalline transparent oxide semiconductor. *Science* 300 (5623): 1269–1272.
- 22 Hosono, H. (2018). How we made the IGZO transistor. *Nature Electronics* 1 (7): 428–428.
- 23 Hosono, H. (2007). Recent progress in transparent oxide semiconductors: materials and device application. *Thin Solid Films* 515 (15): 6000–6014.
- 24 Fortunato, E., Barquinha, P., and Martins, R. (2012). Oxide semiconductor thin-film transistors: a review of recent advances. *Advanced Materials* 24 (22): 2945–2986.
- 25 Mizoguchi, H., Hirano, M., Fujitsu, S. et al. (2002). ZnRh_2O_4 : a *p*-type semiconducting oxide with a valence band composed of a low spin state of Rh^{3+} in a $4d^6$ configuration. *Applied Physics Letters* 80 (7): 1207–1209.
- 26 Narushima, S., Mizoguchi, H., Shimizu, K.I. et al. (2003). A *p*-type amorphous oxide semiconductor and room temperature fabrication of amorphous oxide *p*-*n* heterojunction diodes. *Advanced Materials* 15 (17): 1409–1413.
- 27 Hosono, H. and Kitano, M. (2021). Advances in materials and applications of inorganic electrides. *Chemical Reviews* 121 (5): 3121–3185.
- 28 Matsuiishi, S., Toda, Y., Miyakawa, M. et al. (2003). High-density electron anions in a nanoporous single crystal: $[\text{Ca}_{24}\text{Al}_{28}\text{O}_{64}]^{4+}(4e^-)$. *Science* 301 (5633): 626–629.
- 29 Hosono, H., Kim, J., Toda, Y. et al. (2017). Transparent amorphous oxide semiconductors for organic electronics: application to inverted OLEDs. *Proceedings of the National Academy of Sciences* 114 (2): 233–238.
- 30 Nakamura, N., Kim, J., and Hosono, H. (2018). Material design of transparent oxide semiconductors for organic electronics: why do zinc silicate thin films have exceptional properties? *Advanced Electronic Materials* 4 (2): 1700352.
- 31 Sim, K., Jun, T., Bang, J. et al. (2019). Performance boosting strategy for perovskite light-emitting diodes. *Applied Physics Reviews* 6 (3): 031402.
- 32 Yang, H., Kim, J., Yamamoto, K., and Hosono, H. (2017). Efficient charge generation layer for tandem OLEDs: bi-layered MoO_3/ZnO -based oxide semiconductor. *Organic Electronics* 46: 133–138.
- 33 Jun, T., Kim, J., Sasase, M., and Hosono, H. (2018). Material design of *p*-type transparent amorphous semiconductor, Cu–Sn–I. *Advanced Materials* 30 (12): 1706573.

- 34 Park, J.S., Maeng, W.J., Kim, H.S., and Park, J.S. (2012). Review of recent developments in amorphous oxide semiconductor thin-film transistor devices. *Thin Solid Films* 520 (6): 1679–1693.
- 35 Kwon, J.Y., Lee, D.J., and Kim, K.B. (2011). Transparent amorphous oxide semiconductor thin film transistor. *Electronic Materials Letters* 7 (1): 1–11.
- 36 Nathan, A., Lee, S., Jeon, S., and Robertson, J. (2014). Amorphous oxide semiconductor TFTs for displays and imaging. *Journal of Display Technology* 10 (11): 917–927.
- 37 Yu, X., Marks, T.J., and Facchetti, A. (2016). Metal oxides for optoelectronic applications. *Nature Materials* 15 (4): 383–396.
- 38 Barquinha, P., Martins, R., Pereira, L., and Fortunato, E. (2012). *Transparent Oxide Electronics: From Materials to Devices*. Chichester, UK: John Wiley and Sons.
- 39 Facchetti, A. and Marks, T. (ed.) (2010). *Transparent Electronics: From Synthesis to Applications*. Chichester, UK: John Wiley and Sons.
- 40 Street, R.A. (ed.) (2000). *Technology and Applications of Amorphous Silicon*. Berlin: Springer-Verlag.
- 41 Shiah, Y.-S., Sim, K., Shi, Y. et al. (2021). Mobility-stability trade-off in oxide thin-film transistors. *Nature Electronics* 4: 800–807.

1.2

Transparent Amorphous Oxide Semiconductors

What's Unique for Device Applications?

Hideya Kumomi

Tokyo Institute of Technology, Tokyo, Japan

1.2.1 Introduction

After a long incubation of half a century, the first product of an active-matrix liquid-crystal display (AM-LCD) driven by backplane circuits composed of oxide semiconductor thin-film transistors (TFTs) [1] was commercialized in 2012. Although the manufacturer did not disclose this detail, a small number of the high-resolution (264 ppi) 9.7-inch-diagonal AM-LCD panels on their tablet PC devices (Apple iPad 3) [2] was driven by backplane circuits driven by AOSs, amorphous In-Ga-Zn-O (*a*-IGZO) TFTs. After that, the *a*-IGZO-TFTs were successively commercialized in the AM-LCD screens of smartphones, PC monitors, laptop PCs, and active-matrix organic light-emitting diode (AM-OLED) displays for smartwatches and large-area (up to 88 inches diagonally) and high-resolution (8k×4k) television (TV) screens. Furthermore, even flexible and rollable AM-OLED TVs were launched in October 2020, and *a*-IGZO-TFT-based TVs dominate the AM-OLED TV market. Nowadays, AOS-TFTs have become indispensable component devices for driving active-matrix flat-panel displays (AM-FPDs), along with conventional hydrogenated amorphous Si (*a*-Si:H) TFTs and low-temperature polycrystalline Si (LTPS) TFTs.

It is noteworthy that, even after a half-century incubation of oxide TFTs, *a*-IGZO-TFTs had been commercialized by rapid research and development in a short period of eight years from their first demonstration. It is generally difficult for such a novel and exotic oxide material composed of ternary metal cations to be thrust into an existing industry of established Si-based technologies and to replace a part of them with AOS-TFTs due to both technical and business issues. There are some reasons for the success of *a*-IGZO-TFTs, and these are discussed and elucidated in this chapter based on the technical requirements of electronics industries, along with a historical review of oxide semiconductor-based TFTs and their uniqueness.

1.2.2 Technical Issues and Requirements of TFTs for AM-FPDs

1.2.2.1 Field-Effect Mobility

AM-LCDs at their dawn can be sufficiently driven by *a*-Si:H TFTs that have a small field-effect mobility of $\mu_{FE} \sim 0.1 \text{ cm}^2\text{V}^{-1}\text{s}^{-1}$ because of their low resolutions (i.e., large pixel size), small panel dimensions, and slow frame rates. The μ_{eff} had been enhanced up to $\sim 1 \text{ cm}^2\text{V}^{-1}\text{s}^{-1}$ by improving *a*-Si:H materials, device structures, and fabrication processes to meet the requirements of increasing these specifications and creating greater color depth. However, much higher mobility was required from the beginning of the twenty-first century, when screens larger than 50 inches diagonally and with a higher frame rate than 60 Hz for smooth rendering of movies were demanded by markets. Total capacitance, C , of parasitic capacitance of switching TFTs (T_{sw}) is mainly caused by source-drain

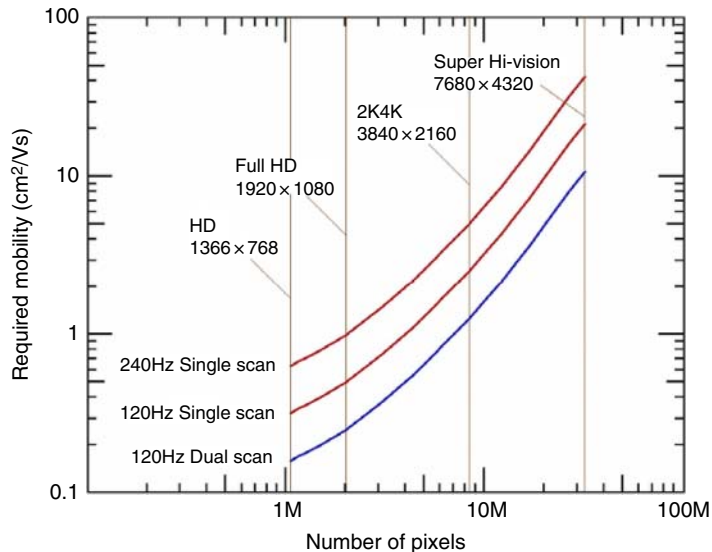


Figure 1.2.1 Dependence of the least mobilities of switching TFTs to drive a 50-inch-diagonal AM-LCD model with a 5- μm -wide Cu gate-line wiring, calculated by Y. Matsueda in 2010 [3]. *Source*: Kamiya, T., Nomura, K., & Hosono, H. (2010). Present status of amorphous In-Ga-Zn-O thin-film transistors. *Science and Technology of Advanced Materials* **11**(4): 044305. doi:10.1088/1468-6996/11/4/044305.

and gate electrodes overlapping, and the storage capacitors in all pixels and so on are parallelly hung on gate (scan)-line metal wirings. Signal transmission from the starting to the ending pixels on a single gate-line must be accompanied by delays with a time constant of RC , where R represents a finite resistance of gate-line wiring determined by the wiring metal materials and their length and cross-sectional areas. This gate-line delay cannot exceed the inverse of the frame rate (i.e., the interval to scan the next gate-line). It is necessary to more rapidly charge the pixel capacitance by enhancing the current driving performance of T_{SW} in order to reduce the gate-line delay. Figure 1.2.1 is a historical plot showing dependence of the least mobilities of T_{SW} to drive a 50-inch-diagonal AM-LCD model with 5- μm -wide Cu gate-line wiring, calculated by Yojiro Matsueda in 2010 [3]. It is estimated here that at least a mobility of $\sim 10 \text{ cm}^2\text{V}^{-1}\text{s}^{-1}$ is required to drive 8k \times 4k panels by a single scan at 120 Hz, which cannot be achieved by the latest high-end α -Si:H TFTs. LTPS-TFTs exhibit high mobilities of $\sim 50\text{--}100 \text{ cm}^2\text{V}^{-1}\text{s}^{-1}$ even when their polycrystalline grain size is far smaller than the TFT channel dimensions to suppress the spatial variety of the TFT properties caused by grain-boundary effects. However, LTPS-TFTs still have difficulties with both short- and long-range uniformity.

In cases of current-driving light-emitting diode (LED) devices like AM-OLEDs, the requirements for driving TFTs (T_{DR}) are added to those for T_{SW} . Various estimations suggest that a mobility of $\sim 10 \text{ cm}^2\text{V}^{-1}\text{s}^{-1}$ is required for T_{DR} to provide sufficient current to the directly connected LED component for sufficient visual brightness independent of FPD resolution and size. This cannot be achieved by α -Si:H TFTs, and thus AM-OLEDs had been produced only for the small-sized panels of smartphones using LTPS-TFT backplanes. Active-matrix electrochromic (EC) displays also happen to require TFTs with a mobility of $\sim 10 \text{ cm}^2\text{V}^{-1}\text{s}^{-1}$ to rapidly charge the EC cells, although they have not been commercialized so far.

Monolithic implementation of peripheral circuits (composed of TFTs like shift-registers for scanning gate-lines and demultiplexers for dividing data signals into RGB subpixels) becomes necessary if the aim is super-high resolution in small panels when it becomes difficult to implement Si-based integrated circuit (IC) chips on the peripherals of AM-FPDs and connect them to the backplane circuits. Especially in mobile devices, the footprint of TFT-based

peripheral circuits should be as small as possible to realize narrow-border frame configurations, and a TFT mobility of $\sim 10\text{--}50\text{ cm}^2\text{V}^{-1}\text{s}^{-1}$ is required to reduce the channel width of the TFTs.

1.2.2.2 Off-State Leakage Current and On/Off Current Ratio

The T_{SW} of AM-FPDs stays in the off-state for most of a frame time after completing the scanning of the gate-line that the T_{SW} is hung on, until the scanning of the gate-line restarts for the next frame. For example, in $8\text{k}\times 4\text{k}$ panels, the T_{SW} remains off for 3,839/3,840 of the time under a relatively high depletion gate bias. Leakage current of the T_{SW} in the off-state should be suppressed to be lower than the reduction of charges in the storage capacitor in one pixel, so as to suppress a change of tone within one bit of color depth. LTPS-TFTs usually exhibit high off-state leakage current and also suffer from inversion operation at a high depletion gate bias; therefore, researchers have attempted to solve this problem by improving their device structures and circuit designs. However, some recent mobile devices try to suppress their power consumption by reducing their frame rate lower than 30 Hz and their power consumption in their peripheral circuits. The lowest frame rate achieved by the LTPS-TFT backplane is only 10 Hz, while AOS-TFTs can easily realize lower than 1 Hz owing to their extremely low off-state leakage current, as described later in this chapter. This feature of low off-state current in AOS-TFTs is actually applied to some mobile products such as smartphones and smartwatches.

Both high mobility and low off-state leakage current lead to enhancement of the on/off current ratio of TFTs. The on/off current ratio should be as large as needed to express necessary color depth if the imaging components are driven by analog control of bias or current. The current standard color depth of eight bits for each primary color has been achieved by conventional Si-based TFTs. However, when higher color depth or a wider color gamut is required, TFTs with a higher on/off current ratio become necessary.

1.2.2.3 Stability and Reliability

TFTs driving AM-FPDs must be stable and reliable against electrical (and thermal) stresses caused by their operation, in addition to thermal, mechanical, and chemical stresses from the environment in electrical devices. The T_{SW} and T_{DR} mainly suffer gate-voltage bias stress and source-to-drain current stress, respectively, and they deteriorate with shifts of TFT characteristics such as threshold voltage, on/off current, and subthreshold swing. TFTs in peripheral circuits are also exposed to various stresses. Some of these shifts can be canceled by special compensation circuits, although the compensation range is limited. Especially in a pixel circuit of AM-OLEDs, characteristics of the OLED component also shift with light-emitting operation, and it is necessary to compensate the characteristic shifts of both TFTs and OLEDs by the compensation circuit composed of the same TFTs. It is very difficult to drive AM-OLEDs with a backplane circuit based on unstable α -Si:H TFTs, in addition to the difficulty in driving OLEDs with their small mobilities. Therefore, early products of AM-OLED displays were driven by backplane circuits composed of stable LTPS-TFTs, which limit mother-glass sizes (smaller than generation 6 [Gen. 6]) in mass production and thus final panel sizes up to several inches in diagonal.

1.2.2.4 Uniformity

Characteristics of TFTs driving AM-FPDs should be uniform over their panel dimension to guarantee uniform brightness, colors, and tone rendering. Spatial variations of characteristics of LTPS-TFTs are relatively large due to the in-plane inhomogeneity of polycrystalline grain boundaries, where carrier transfer is hindered by high potential barriers, and the short-range uniformity among neighboring TFTs is not good. Neither is the long-range uniformity between distant TFTs over panel dimensions because of the inhomogeneous formation process with scanning a line-shaped and short-pulsed excimer-laser annealing (ELA) for the melting and recrystallization process of α -Si thin films. On the other hand, α -Si:H TFTs show good uniformity in both short and long ranges owing

to their amorphous nature, with no grain boundaries or film formation by plasma-enhanced chemical-vapor deposition (PECVD). Therefore, middle- and large-area (≥ 10 inches in diagonal) AM-FPDs have been driven by *a*-Si:H TFT-based backplanes.

1.2.2.5 Large-Area Devices by Large-Area Mother-Glass Substrates

In addition to the uniformity issues in LTPS-TFTs that have been discussed so far in this chapter, there is another reason for difficulty in enlarging mother glasses beyond Gen. 6, and thus in enlarging the final panel size over several inches in diagonal in mass production. In the fabrication processes of LTPS-TFTs, *a*-Si:H thin films are formed over glass substrates by PECVD first, and then the high-density hydrogens in the films have to be removed (dehydrogenation) before the subsequent ELA process to avoid explosion of the films by hydrogen vaporization. The dehydrogenation requires thermal annealing for several hours at a temperature higher than ~ 450 °C. The high-temperature annealing demands special and expensive glass substrates with very small thermal deformation, but these are not available for mother glasses larger than Gen. 6. Furthermore, it is also difficult to expand the length of line-shaped excimer-laser beams in ELA beyond the dimension of the Gen. 6 mother glasses. Because the cost of an AM-FPD panel is most strongly determined by the number of panels cropped from one mother glass, AM-FPD panel products based on LTPS-TFTs are limited to small-sized (a few to several inches in diagonal) ones, such as those for smartphones.

Mother-glass substrates larger than Gen. 6 (up to >10) had been available to *a*-Si:H TFTs, because the highest process temperature is ~ 350 °C in PECVD of *a*-Si:H thin films and gate-insulator films, and there is no limitation to substrate sizes in PECVD. Large-sized AM-FPDs had been supplied exclusively with backplanes based on *a*-Si:H TFTs. As mentioned in this chapter, however, there are many AM-FPDs that cannot be driven by *a*-Si:H TFTs, and these had not been commercialized.

1.2.2.6 Low-Temperature Fabrication and Flexibility

A far lower fabrication-processing temperature than ~ 350 °C is indispensable if substrates are not heat-resistant. Most of the substrates based on polymer plastic sheets for flexible devices cannot endure thermal stresses at temperatures higher than ~ 200 °C. Some emerging semiconductor materials, such as organic molecules, carbon nanotubes, graphene, transition metal dichalcogenide, halide perovskite, and so on, could be fabricated at low temperatures down to room temperature, but none of them can meet the other requirements mentioned here.

Characteristics of TFTs on flexible devices also have to be stable under fixed or repeated mechanical stresses of bending. Curved or foldable AM-OLED panels driven by LTPS-TFTs are commercialized on smartphones, but further flexible products with rollable panels have not been launched until recently.

1.2.3 History, Features, Uniqueness, Development, and Applications of AOS-TFTs

1.2.3.1 History

In 1939, William Shockley attempted a demonstration of transistors using Cu_2O [4], which is regarded as the earliest challenge to oxide semiconductor-based active devices. Unfortunately, the Cu_2O transistor never operated, so he changed the semiconductor material to germanium (Cu_2O TFTs still do not operate, even in 2021). The first TFT was demonstrated in 1962 using a chalcogenide semiconductor, CdS [5]. The first TFTs using oxide semiconductors, SnO_2 and In_2O_3 , appeared in 1964 [6], which was two years earlier than the appearance of polycrystalline Si-based field-effect transistors (FETs) in 1966 [7]. FETs based on single-crystalline ZnO followed these pioneers

as a demonstration of oxide semiconductor-based transistors in 1968 [8]. However, further followers have not appeared for more than three decades since then. This was probably due to a lack of killer applications of TFTs during that era. On the other hand, *a*-Si:H thin films emerged in the 1970s [9], and many researchers rushed into them because of their potential applications in backplane circuits for AM-FPDs and in photosensitive and photovoltaic devices, and because of scientific interest in their local and electronic structures. Since the first AM-LCD with an *a*-Si:H TFT backplane was proposed in 1981 [10], Si-based TFTs including polycrystalline Si TFTs dominated the commercialization of AM-FPDs for decades until quite recently. Thus, oxide TFTs had fallen into oblivion for a long time, while oxide semiconductors such as In-Sn-O have played an important role to date as conductors in applications with transparent electrodes.

What re-ignited interest in oxide semiconductors was a working hypothesis, proposed in 1996, about candidate materials for high-mobility amorphous oxides [11]. The hypothesis predicts that oxides of post transition metals with an electronic configuration of $(n-1)d^{10}s^0$ could exhibit high electron mobility, even in amorphous phases. The actual material used in the operation of high-performance TFTs was demonstrated several years later. Meanwhile, oxide semiconductor-based TFTs were revived by aiming at AM-FPD applications via a demonstration of solution-processed polycrystalline ZnO-TFTs in 2001 [12], which was followed by sputter-deposited ZnO-TFTs by many researchers. However, ZnO-TFTs have not been commercialized so far because they cannot escape serious technical issues caused by polycrystalline grain boundaries, and a superior alternative appeared later. In 2003, Nomura *et al.* demonstrated that a multicomponent oxide TFT showed a high field-effect mobility of $\mu_{FE} \sim 80 \text{ cm}^2\text{V}^{-1}\text{s}^{-1}$, using *c*-axis-oriented crystalline $\text{InGaO}_3(\text{ZnO})_5$ (IGZO) thin films formed by reactive solid-phase epitaxy at high temperature [13]. During exploration of the candidates predicted by the working hypothesis [12], with an insight into electronic configurations and the role of Ga cations, this material system was discovered to be a high-mobility oxide semiconductor. Actually, the first AOS-TFTs were demonstrated in 2004 with $\mu_{FE} \sim 9 \text{ cm}^2\text{V}^{-1}\text{s}^{-1}$, using amorphous In-Ga-Zn-O (*a*-IGZO) thin films deposited on plastic substrates at room temperature [14].

AOS-TFTs have attracted keen attention, mainly because their channel mobilities are ~ 10 times higher than those of conventional *a*-Si:H TFTs. After a few years since the first demonstration of *a*-IGZO-TFTs, an explosive increase in their research and development started, with numerous publications [15]. Finally, in 2012, after remaining in obscurity for over half a century since the first demonstration, the first commercial product based on AOS-TFTs was launched in the worldwide market in a small number of mobile electronic devices. Since then, *a*-IGZO-TFTs have been mainstayers of oxide semiconductors commercialized in electronic device products due to their useful nature.

1.2.3.2 Features and Uniqueness

As mentioned in Section 1.2.3.1, the choice of complicated quaternary compounds like IGZO—rather than simple binaries like ZnO, SnO_2 , and In_2O_3 —is based on a working hypothesis for high-mobility amorphous oxides [11]. In these binary compounds, it is difficult to control oxygen deficiencies and to reduce intrinsic carrier density to suppress the off-current and instability of their TFTs. Furthermore, the choice of quaternary compound is based on insight into the coordination number of Ga in IGZO, where Ga^{3+} does not replace Zn^{2+} taking fivefold coordination to suppress excess carrier generation, while Ga^{3+} doped into ZnO replaces Zn^{2+} taking fourfold coordination to generate carriers. Thus, *a*-IGZO was selected as a model compound of candidates for channel materials of high-performance TFTs.

AOS thin films and their TFTs like *a*-IGZO have the following features and uniqueness:

1. Most AOS materials are *n*-type semiconductors.
2. Carrier mobility increases with carrier density via a percolation transport mechanism, unlike conventional crystalline semiconductors with covalent bonding.

3. Films are transparent to the light in a range of visible wavelengths due to wide band gaps ($E_g \gtrsim 3$ eV).
4. It is possible to form the channel layers over noncrystalline substrates at low temperature by sputtering deposition, molecular–organic chemical vapor deposition, atomic layer deposition, and solution process coating.
5. Various conventional gate-insulator materials are available with low densities of interfacial trap states, which warrant sufficiently high breakdown voltages for various applications.
6. It is easy to form good ohmic contact to various source–drain electrodes.
7. Uniformity in both short and long ranges is excellent because the films are free from crystalline grain boundaries.
8. Operation mechanisms are relatively simple so that TFT models for device and circuit simulations are simple. See Chapter 16 for some examples.
9. The features in (4)–(8) enable us to adopt methods and facilities for device and circuit designs and manufacturing, which have been used for Si-based TFTs.
10. A lower tail-state density beneath the conduction band minimum than *a*-Si:H TFTs by a few orders of magnitude makes large band vending possible to push up the Fermi level into the conduction band by field effect at low voltages of a forward gate bias. This leads to operations with band-like transport exhibiting over 10 times higher channel mobilities and low threshold voltages.
11. A low-subgap deep-level density of states (DOS) above the midgap level enables fast switching with a small subthreshold swing (~ 0.1 V·dec⁻¹).
12. A large occupied DOS below the midgap level and above the valence band maximum hinders band vending to pull down the Fermi level into the valence band under a backward gate bias. It also prohibits an inversion operation, which leads to very low off-current.
13. The feature of (12) also suppresses a kink effect in the output characteristics of TFTs.
14. Hot-carrier effect and short-channel effect are also small, and source-to-drain breakdown voltages are high.
15. Stability and reliability under electric or mechanical stresses are much better than those of *a*-Si:H TFTs and comparable to those of LTPS-TFTs.

Furthermore, especially for *a*-IGZO:

16. TFT performance is good around metal cation compositions of crystalline single phases such as In:Ga:Zn:O=1:1:1:4 or 2:2:1:7, and it slowly changes with composition around these single phases.
17. Large-area, stable, polycrystalline sputtering targets with single-phase crystalline compositions are available due to (16).

The features of (10) and (11) just meet the technical requirements for field-effect mobility (see Section 1.2.2.1). The features of (10) and (12) satisfy the requirements for off-state leakage current and on/off current ratio (Section 1.2.2.2). The features of (13), (14), and (15) fulfill the conditions for stability and reliability (Section 1.2.2.3). The feature of (7) meets the needs for uniformity (Section 1.2.2.4). The features of (9) (i.e., (4)–(8)), (16), and (17) satisfy the requirement for large-area devices by large-area mother-glass substrates (Section 1.2.2.5). The features of (4) and (15) fulfill the requirement for low-temperature fabrication and flexibility (Section 1.2.2.6). These are the reasons that AOS-TFTs have been actively researched, developed, and commercialized.

While the features and uniqueness of AOS thin films and their TFTs give great advantages to their applications, there are still two major issues remaining to be solved. The first one is instability under light illumination, even in a range of visible wavelength with energy smaller than E_g despite transparency. The illumination of light shorter than half of E_g excites the deep occupied states below the midgap (featured in (11)) and generates electron–hole pairs to cause persistent photoconductivity and shift threshold voltage, V_{TH} , to the negative direction. Furthermore, when the TFT is stressed by a negative gate bias simultaneously with an illumination stress, V_{TH} largely shifts to the negative direction. This phenomenon is called instability under negative-bias-illumination stress (NBIS) and explained by the following mechanism: The positive charge carriers like holes are drifted toward the

interface to the gate insulator through a band bending by the negative gate bias and finally trapped by the interfacial states, and as a result, the effective gate-bias voltage is shifted in the positive direction and V_{TH} moves in the negative direction. The NBIS instability is a serious problem, especially for a switching TFT in a pixel circuit of an AM-LCD, which is biased by a large negative gate voltage for most of a frame time and always illuminated with the bright LCD backlight. The instability issues under illumination have been so far solved in commercial products by introducing some light-shielding structures into TFT device layers. Essential solutions to these problems have been proposed, such as adopting much wider E_g AOS materials [16], but they have not satisfied all of the other properties shown in the features of (1)–(17) that are required for AM-FPD applications.

The second one is a much higher μ_{FE} than $\sim 10 \text{ cm}^2\text{V}^{-1}\text{s}^{-1}$. As mentioned in Section 1.2.2.1, dimensions of peripheral circuits in AM-FPDs depend on the width of channels of implemented TFTs. Higher μ_{FE} reduces the channel width and the width of the peripheral circuits to realize narrower borders of AM-FPDs. It is estimated that $\mu_{FE} \gtrsim 30 \text{ cm}^2\text{V}^{-1}\text{s}^{-1}$ is necessary to design the border width narrower than a few millimeters. Many challenges have been made, such as In-rich compositions in α -IGZO or amorphous In-Sn-Zn-O (ITZO), and some of them have started to be adopted in commercial products.

1.2.3.3 Applications

After their revival in the twenty-first century, active research of oxide semiconductor-based TFTs aiming at potential applications started with intense motivation due to their advantages, as described in Section 1.2.3.2. Figure 1.2.2 shows the emergence, evolution, and transition of application targets in the first decade, starting with the first demonstration of α -IGZO-TFTs in 2004.

Initially, early challengers attempted to apply AOS-TFTs for AM-FPD backplane circuits of electric papers using electrophoretic display (EPD) devices on flexible polymer substrates, especially for low-temperature fabrication

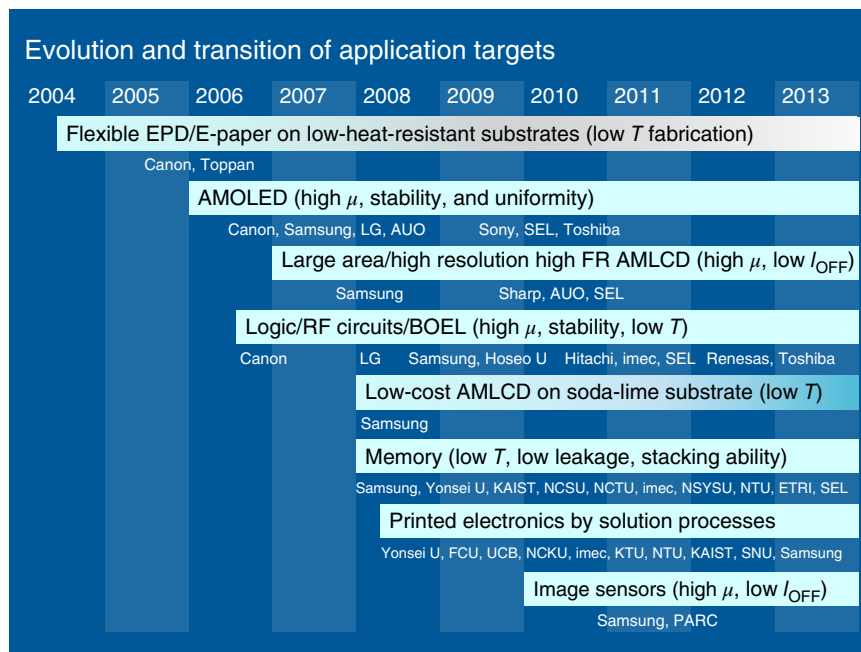


Figure 1.2.2 Emergence, evolution, and transition of application targets in the first decade of the twenty-first century, starting with the first demonstration of α -IGZO-TFTs in 2004.

processes. However, no commercial products have been launched because high-mobility TFTs are not always necessary for EPDs that are not able to show movies and full-color pictures due to their slow response and low contrast, and the market for electric papers has not grown.

Applications to AM-OLED backplanes also started from the early days, taking advantage of high mobility, high stability, and high uniformity. As mentioned in Section 1.2.2, it is difficult to drive and fabricate large-sized AM-OLED panels by α -Si:H and LTPS-TFTs, respectively, and new, more competent TFTs have been long desired. AOS-TFTs only recently met the demands of large-sized AM-OLEDs, and commercial TV products appeared in 2015. Applications to advanced AM-LCDs with higher pixel resolutions, frame rate, and color depth followed those of AM-OLEDs, utilizing various advantages of AOS-TFTs, and the first commercial product was launched in 2012. The current leading research is introduced in Chapters 15 and 18.

There were some challenges to apply AOS-TFTs to low-cost AM-LCDs fabricated at low temperatures on low-cost soda-lime glass substrates that cannot suffer high-temperature processes, instead of expensive and heat-resistant alkaline-free glass substrates. These challenges have failed to date, because it was found that post-annealing at $\geq 300^\circ\text{C}$ was necessary to reduce defect densities of AOS thin films for TFT backplanes of AM-FPDs.

Low-power-consumption AM-FPDs, which can reduce frame rates when displayed pictures are immobile, also have been proposed based on the extremely low off-leakage current of AOS-TFTs. The lower the frame rate is, the lower the power consumption in the peripheral circuits is. The low frame rate driving by AOS-TFTs has been commercialized in mobile devices such as smartphones and smartwatches.

There have been many challenges except applications to AM-FPDs. The high mobility and low-temperature fabrication of AOS-TFTs facilitate their applications to logic and radiofrequency circuits on flexible polymer substrates for wireless communications. The state-of-the-art research is introduced in detail in Chapter 17. High breakdown voltage and low-temperature fabrication encourage engineers and scientists engaged in Si-based ultra-large-scale integration (ULSI) circuits to apply AOS-TFTs to the peripheral back-end-of-line circuits of ULSI. The leading research is described in Chapter 20. Volatile and nonvolatile memory devices comprise one of the most promising candidates for AOS-TFT applications, and they have been investigated utilizing low leakage current and low-temperature fabrications. The details are described in Chapters 19, 20, and 21. Neuromorphic applications based on AOS thin-film devices have also attracted attention, and they are described in Chapter 22. Application of AOS-TFT-based active-matrix backplanes to X-ray image sensor arrays is described in Chapter 23. These post-AM-FPD applications are expected to be commercialized soon, taking advantage of accumulated technologies for materials, designs, and fabrications developed in AM-FPD applications.

1.2.3.4 Development and Products of AM-FPDs

Through active research on applications (mentioned in Section 1.2.3.3), many prototype AM-FPDs have been demonstrated using backplanes composed of oxide semiconductor TFTs. Three small panels initially appeared in the same year of 2006: (i) Ito *et al.* demonstrated a color EPD driven by transparent α -IGZO-TFTs formed over color filter arrays on a polymer substrate at room temperature [17], (ii) Hirao *et al.* demonstrated a transparent AM-LCD panel driven by ZnO-TFTs [18], and (iii) Park *et al.* demonstrated a transparent AM-OLED panel driven by ZnO-TFTs [19]. These pioneering works were then followed by worldwide activities in academies and industries to demonstrate more sophisticated prototype panels mainly using α -IGZO-TFTs with enhancement of panel size, resolution, color rendering, and flexibility.

During this prototyping period, the remaining technical problems of stability, device structures, and mass production had been solved. Finally, in 2012, the first commercial product was launched into market in a small number of shipping tablet PC products (Apple iPad 3) with high-resolution (264 ppi) 9.7-inch-diagonal AM-LCDs for their screen panels driven by the α -IGZO-TFT-based backplane circuits. Since then, high-resolution AM-LCDs driven by α -IGZO-TFTs have been adopted by some smartphones, PC monitors, laptop PCs, and tablet PCs. In 2015, LG launched the first AM-OLED product, a 55-inch-diagonal full-high-definition (FHD; 2k) TV with a curved



Figure 1.2.3 Market-leading product of a 65-inch-diagonal 4k AM-OLED TV, donated by the manufacturer to the inventor of α -IGZO-TFTs.

panel driven by α -IGZO-TFTs. The AM-OLED TV products have evolved to a larger size (up to 88 inches diagonal) and a higher resolution (up to ultra-high-definition [UHD]; 8k), and they are more flexible with rollable screens through 2021 (Figure 1.2.3). Hybrid backplanes composed of both LTPS- and α -IGZO-TFTs (called “LTPO-TFTs”) have also been proposed to partially use AOS-TFTs for frame-rate reduction, and they have been adopted in AM-OLED panels of smartwatch products (since the Apple Watch Series 4 in 2018), where power-consumption savings are critical due to the watches’ small batteries and the panels display motionless pictures very often. The LTPO-TFT-based AM-OLED panels also will soon be adopted by smartphones to boost the highest frame rate over 120 Hz and enhance user experiences in motion pictures, gaming, and artificial/virtual-reality content by suppressing response delays.

It is expected that AOS-TFTs will drive emerging and promising AM-FPDs such as halide perovskite LED (PeLED) and micro-LED (μ LED) displays. Requirements for backplane TFTs from PeLED displays are almost the same as and rather simpler than AM-OLEDs. Current AOS-TFTs will readily meet the needs of high-performance PeLED displays when they are developed to acquire sufficient stability. On the other hand, μ LED displays are composed of arrays of discrete GaN-based LEDs that have too steep a turn-on threshold to control by an analog driving scheme with continuous variation of injected current, and they have to be controlled by digital driving of pulse-width modulation (PWM). The PWM requires very abrupt changes in currents and very high mobilities for driving transistors. Therefore, much higher mobility AOS-TFTs than the current α -IGZO are required.

1.2.4 Summary

After incubation for over a half century, oxide semiconductor TFTs were commercialized by research and development of AOS-TFTs for only eight years from the emergence of α -IGZO-TFTs. Such relatively quick commercialization is due to not only the excellent properties of AOSs and their fortunate and timely fit with the technical requirements of applications, but also low barriers to entry into AOS-based technologies and commercialization, which are protected by fundamental intellectual properties licensed nonexclusively to everyone. AOSs have become one of the platform materials for semiconductor devices today.

There are still remaining issues in AOSs, as briefly mentioned, but it is expected that, after solving them, AOSs will become much more important in AM-FPD technologies and be used in other applications.

References

- 1 Kamiya, T., Nomura, K., and Hosono, H. (2010). Present status of amorphous In–Ga–Zn–O thin-film transistors. *Science and Technology of Advanced Materials* 11: 044305-1–044305-23.
- 2 <https://support.apple.com/en-us/HT201471#ipad>
- 3 Matsueda, Y. (2010). Required characteristics of TFTs for next generation flat panel display backplanes. *Digest of International Thin-Film Transistor Conference 2010*: S6.
- 4 Shockley, W. (1976). The path to the conception of the junction transistor. *Transactions on Electron Devices* ED-23: 597.
- 5 Weimer, P.K. (1962). The TFT: a new thin-film transistor. *Proceedings of the IRE* 7: 1462–1469.
- 6 Klasens, H.A. and Koelmans, H. (1964). A tin oxide field-effect transistor. *Solid-State Electronics* 7: 701–702.
- 7 Fa, C.H. and Jew, T.T. (1966). The poly-silicon insulated-gate field-effect transistor. *IEEE Transactions on Electron Devices* ED-13: 290–291.
- 8 Boesen, G.F. and Jacob, J.E. (1968). ZnO field-effect transistor. *Proceedings of the IEEE* (November): 2094–2095.
- 9 Spears, W.E. and LeComber, P.G. (1972). Investigation of the localised state distribution in amorphous Si films. *Journal of Non-Crystalline Solids* 8–10: 727–738.
- 10 Snell, A.J., Mackenzie, K.D., Spears, W.E. et al. (1981). Application of amorphous silicon field effect transistors in addressable liquid crystal display panels. *Applied Physics* 24: 357–362.
- 11 Hosono, H., Yasukawa, M., and Kawazoe, H. (1996). Working hypothesis to explore novel wide band gap electrically conducting amorphous oxides and examples. *Journal of Non-Crystalline Solids* 198–200: 165–169.
- 12 Ohya, Y., Niwa, T., Man, T., and Takahashi, Y. (2001). Thin film transistor of ZnO fabricated by chemical solution deposition. *Japanese Journal of Applied Physics* 40: 297–298.
- 13 Nomura, K., Ohta, H., Ueda, K. et al. (2003). Thin-film transistor fabricated in single-crystalline transparent oxide semiconductor. *Science* 300: 1269–1272.
- 14 Nomura, K., Ohta, H., Takagi, A. et al. (2004). Room-temperature fabrication of transparent flexible thin-film transistors using amorphous oxide semiconductors. *Nature* 432: 488–492.
- 15 Fortunato, E., Barquinha, P., and Martins, R. (2012). Oxide semiconductor thin-film transistors: a review of recent advances. *Advanced Materials* 24: 2945–2986.
- 16 Kim, J., Sekiya, T., Miyokawa, N. et al. (2017). Conversion of an ultra-wide bandgap amorphous oxide insulator to a semiconductor. *NPG Asia Materials* 9: e359-1–e359-7.
- 17 Ito, M., Kon, M., Ishizaki, M. et al. (2006). A novel display structure for color electronic paper driven with fully transparent amorphous oxide TFT array. *Proceedings of the IDW/AD '06* EP1-4L: 585–586.
- 18 Hirao, T., Furuta, M., Furuta, H. et al. (2006). Distinguished paper: high mobility top-gate zinc oxide thin-film transistors (ZnO-TFTs) for active-matrix liquid crystal displays. *SID Symposium Digest of Technical Papers* 37 (4.1): 18–20.
- 19 Park, S.-H.K., Hwang, C.-S., Lee, J.-I. et al. (2006). Transparent ZnO thin film transistor array for the application of transparent AM-OLED display. *SID Symposium Digest of Technical Papers* 37 (4.3): 25–28.

Part II

Fundamentals

2

Electronic Structure and Structural Randomness

Julia E. Medvedeva^{1,†}, Bishal Bhattarai¹, and D. Bruce Buchholz²

¹Department of Physics, Missouri University of Science and Technology, Rolla, Missouri, USA

²Department of Materials Science and Engineering, Northwestern University, Evanston, Illinois, USA

2.1 Introduction

Structural disorder has been known to suppress carrier concentration and carrier mobility in common covalent semiconductors, such as silicon, by orders of magnitude. The lack of periodicity and bond irregularities in the amorphous phases with strong directional bonding reduces the orbital overlap of the neighboring atoms and give rise to the formation of localized defect states near the band edges that may cause electron trapping, carrier scattering, and subgap absorption. In striking contrast to the covalent semiconductors, oxides of posttransition metals with ionic bonding are known to remain transparent in the visible range and exhibit not only crystalline-like electron mobility upon amorphization, but also 1–2 orders of magnitude higher carrier concentration in the disordered phases as compared to their crystalline counterparts [1–10].

The weak ionic bonding between posttransition metals and oxygen atoms makes the structural description of the amorphous oxide semiconductors (AOSs) challenging. In marked contrast to the Si- or Ge-based semiconductors or SiO₂-based glasses (composed of the main-group metal oxides) that have strong covalent bonding responsible for distinct symmetry-defined nearest-neighbor polyhedra, the weak ionic metal–oxygen (M–O) bonds in AOSs allow for large bond length and angle deviations resulting in strong distortions in the M–O polyhedra and, therefore, in significant disorder within the short-range (nearest-neighbor) structure. These deviations must be carefully quantified in order to determine their role in the electronic properties of AOSs. For this, theoretical and experimental characterization that involves statistical averaging, although instructive in predicting some macroscopic properties such as optical band gap and electron effective mass using established solid-state theories, will miss important information hidden in the distribution and its tails. It might seem reasonable to assume that the structural outliers are key to understanding carrier generation and carrier scattering in AOSs; the larger the structural deviation from an average or a crystalline value, the more localized the defect should be. However, there is a second important consequence of the weak bonding in AOSs that must be taken into account in order to understand the resulting electronic properties: An undercoordinated atom or a strongly distorted polyhedron may trigger significant bond reconfiguration not only in the immediate vicinity, but also throughout the weakly bound disordered network via a ripple effect. As a result, the AOS's susceptibility to long-range structural rearrangement is beneficial for carrier transport: It may not only improve hybridization of different constituents (e.g., in a multi-cation oxide) in the conduction states, but also *reduce* the electron scattering via extensive structural reconfiguration near defects, dopants, or impurities [11–13]. The latter is not possible in crystalline oxides where the translational periodicity of the well-defined lattice limits structural relaxation around a defect to its nearest or next-nearest neighbors.

† In loving memory of my father, Evgeny Medvedev, who gave me boundless support and encouragement.

Amorphous Oxide Semiconductors: IGZO and Related Materials for Display and Memory, First Edition.

Edited by Hideo Hosono and Hideya Kumomi.

© 2022 John Wiley & Sons Ltd. Published 2022 by John Wiley & Sons Ltd.

Therefore, structural outliers in AOSs should be considered along with their environment—a disordered, random structure—that requires a systematic description in order to gain insights into carrier generation and mobility in AOSs.

Traditionally, the structural characterization of disordered oxides focuses on the M-O and M-M distributions; however, it is critical to understand how disorder affects the oxygen environment. Owing to the directional nature of the O-*p*-orbitals, the distortions in the O-M polyhedra are expected to have a more pronounced effect on the electronic properties of AOSs as compared to the symmetry-indifferent spherical *s*-orbitals of the posttransition metals [14]. Indeed, the differences in the orbital sensitivity to disorder are manifested in the characteristic asymmetry of the electronic localization of the tail states near the band edges in AOSs: The top of the valence band formed from the O-*p*-states exhibits strongly localized states, whereas the *s-p*-hybridized conduction states are generally delocalized in stoichiometric or nearly stoichiometric amorphous oxides and may feature shallow or weakly localized defects associated with metal undercoordination, even in highly sub-stoichiometric oxides [11]. The localized tail states near the top of the valence band arise from nonbonding O-*p*-orbitals for the oxygen atoms that are undercoordinated or in a highly distorted nearest-neighbor (metal) environment. These localized O-*p*-states were shown to contribute to the visible-range absorption in stoichiometric amorphous In₂O₃ [11] and play a key role in H defect formation and H mobility in amorphous In-Ga-O doped with hydrogen [12, 13]. While the most advanced X-ray scattering techniques for short-range structural characterization are not sensitive enough to probe the coordination environment of lightweight oxygen atoms, *ab initio* modeling combined with X-ray photoelectron spectroscopy (XPS) O1s or with oxygen nuclear magnetic resonance (NMR) measurements should provide valuable insights into oxygen coordination distribution and its role in the electrical and optical properties of AOSs.

Many important aspects of AOSs have been addressed theoretically. The first molecular dynamics (MD) simulations of amorphous indium oxide appeared in 2009 [15], followed by models of electron transport in multi-cation AOSs [16–21], density functional theory (DFT) calculations of defect formation [22–29], and statistical descriptions of amorphous networks [30–32]. Despite the tremendous progress, the structural randomness that leads to an intricate interplay between bond distortions, coordination morphology, and electron (de)localization in AOSs is far from being understood.

In this work, computationally intensive *ab initio* MD simulations, comprehensive structural analysis, and hybrid density-functional calculations are employed to accurately describe the peculiarities in short- and medium-range structures of amorphous In₂O₃, SnO₂, ZnO, and Ga₂O₃ and their role in the resulting electronic properties. In addition to carefully considering the statistical distributions of the nearest- and next-nearest-neighbor structural characteristics for both metal and oxygen atoms, we examine the individual M and O features and compare the results to the corresponding values in the crystalline oxides. To establish rigorous structure–property relationships, we calculate a so-called effective coordination number (ECN) for every atom based on a weighted average distance in the given polyhedron [33]. This approach provides a significant improvement of the structural description of the ionic AOSs as compared to the typical cutoff-based calculations that neglect bond distribution in individual polyhedra and hence may under- or overestimate the coordination for a large fraction of atoms. Similarly, we avoid the traditional electronic structure tools, such as atom-resolved density-of-states calculations that also rely on a fixed cutoff radius neglecting nonspherical charge density distribution near low-coordinated atoms or those in highly distorted environments. Instead, we employ Bader charge analysis that assigns charge values based on the carefully calculated gradients in the charge density distribution around each atom [34, 35]. Relating the structural peculiarities of each individual atom to its Bader charge contribution in the valence and conduction band helps us establish the microscopic origins of the electron (de)localization in the disordered oxide materials—and develop a framework for an accurate description of complex AOSs’ behavior. In addition to the four binary oxides that are common constituents in the AOS phase space, we extend our analysis to multicomponent In-Ga-O (IGO) and In-Ga-Zn-O (IGZO) to highlight how metal composition affects the intricate structure–property relationships of AOSs with tunable properties.

2.2 Brief Description of Methods and Approaches

2.2.1 Computational Approach

All amorphous oxide structures were obtained using an *ab initio* MD liquid-quench approach, as implemented in the Vienna Ab Initio Simulation Package (VASP) [36, 37]. The calculations are based on DFT with periodic boundary conditions and employ Perdew–Burke–Ernzerhof (PBE) exchange–correlation functionals [38] within the projector augmented-wave method [39, 40]. An initial stoichiometric oxide structure with specific density was melted at 3000 K to eliminate any crystalline memory and randomize the composition. The melting step was followed by quench cycles with a specific cooling rate and an equilibration MD step at room temperature to stabilize the amorphous structure. Next, each atomic configuration was fully relaxed using DFT-PBE at 0 K. For optimization, the cutoff energy of 500 eV and the $4\times 4\times 4$ Γ -centered k -point mesh were used; the atomic positions were relaxed until the Hellmann–Feynman force on each atom was below 0.01 eV/Å. The electronic and optical properties of amorphous In-based oxides were calculated using the hybrid Heyd–Scuseria–Ernzerhof (HSE06) approach [41] with a mixing parameter of 0.25 and a screening parameter μ of 0.2 Å⁻¹.

To obtain adequate statistical distributions in the structural and, consequently, the electronic properties, 10–20 separate MD liquid-quench realizations with the same parameters and conditions (density, composition, stoichiometry, initial temperature, quench rate, equilibration, and relaxation) were obtained for each system. The density of an amorphous structure is an important factor and must be carefully determined. A set of independent MD liquid-quench simulations were performed for 4–5 different density values for each composition, resulting in over 300 MD realizations performed for this work. Upon room-temperature equilibration, the DFT total energy was calculated as an average over the final 500 MD steps to remove thermal fluctuations and plotted as a function of density for each oxide.

To validate the MD simulated structures, we calculate the extended X-ray absorption fine-structure (EXAFS) spectra for all amorphous models [42, 43] to directly compare the results with available experimental EXAFS measurements that capture the changes in the M–O bond lengths as well as in the second-shell M–M characteristics responsible for the medium-range structure at different densities.

Structural randomness in amorphous oxides is then quantified by analyzing the characteristics of individual atoms. For this, the effective average distance (l_{av}) for the M–O (O–M) first shell for each M–O (O–M) polyhedron was calculated using a weighted average, where each M–O (O–M) bond distance is compared to the shortest M–O (O–M) distance in each given polyhedron [34, 35]. Next, the ECN for individual M and O atoms was calculated as a sum of the first-shell distances weighted with respect to the effective average length obtained for each polyhedron. In addition, we calculate the distortion of each M–O (O–M) polyhedron σ^2 , characterized by the standard deviation of the individual M–O bond lengths from the effective average M–O bond length for the given polyhedron. As mentioned in Section 2.1, this approach provides a significant improvement for the structural analysis of the ionic AOSs as compared to the typical approach that uses a single cutoff distance for all polyhedra, thus neglecting bond distribution in individual polyhedra, and hence may under- or overestimate the coordination of a large fraction of atoms in AOSs.

In addition, the total and partial vibrational density-of-states (VDOS) calculations were performed for the optimized structures to provide crucial information about local bonding and the dynamical stability of a model. The vibrational inverse participation ratio (VIPR) was calculated from the normalized displacement vectors to determine the localization of different vibrational modes. Finally, optical absorption was derived from the frequency-dependent dielectric function calculated within independent particle approximation using the electronic transitions of the hybrid functional (HSE06) solution. The atomic structures and charge densities were plotted using VESTA software [44].

2.2.2 Experimental Approach

Amorphous binary oxide thin films were grown by pulsed-laser deposition (PLD) from dense hot-pressed indium oxide, zinc oxide, tin oxide, or gallium oxide targets (25 mm diameter). PLD was accomplished with a 248 nm KrF excimer laser with 25 ns pulse duration and operated at 2 Hz. The 200 mJ/pulse beam was focused onto a 1 mm \times 3 mm spot size. The target was rotated at 5 rpm about its axis to prevent localized heating. The target-substrate separation was fixed at 10 cm. Both the amorphous and crystalline films were grown at O₂ ambient pressure of 7.5 mTorr. The silica substrates were attached to the substrate holder with silver paint and grown at a specific deposition temperature to ensure the films are amorphous. Films grown above 25 °C were attached to a resistively heated substrate holder; films grown below 25 °C were attached to a liquid nitrogen-cooled substrate holder. The amorphous In₂O₃, SnO₂, and Ga₂O₃ films were grown at -25 °C. The amorphous ZnO film was grown at -100 °C. All crystalline films were grown at +600 °C.

X-ray absorption spectroscopy (XAS) was performed at the 5-BMD (bending-moment diagram) beam line of DND-CAT (the DuPont-Northwestern-Dow Collaborative Access Team) at the Advanced Photon Source (APS) of Argonne National Laboratory (Argonne, IL). Metal $k\alpha$ fluorescence emissions from the metal-oxide thin films were measured using a four-element Si-drifted detector (SII) with the incident X-ray angle θ at about 45° with respect to the sample surface. The data were Fourier transformed with a Hanning window over multiple k ranges, where one-shell and three-shell fits were examined. The k ranges of the EXAFS data used in the analyses were $k = 2.5$ to 11.972 \AA^{-1} (ZnO), 2.0 to 15.5 \AA^{-1} (In₂O₃), 1.0 to 14.0 \AA^{-1} (Ga₂O₃), and 2.3 to 15.8 \AA^{-1} (SnO₂), with a k -weight of 3.

2.3 The Structure and Properties of Crystalline and Amorphous In₂O₃

First, the total pair-correlation functions for crystalline (bixbyite) and amorphous stoichiometric In₂O₃ with different densities are shown in Figure 2.1a. Both crystalline and amorphous results were obtained from the MD simulations at 300 K (equilibration with 3,000 MD steps or 6 ps) to include possible temperature fluctuations. The results for amorphous structures represent an average over at least 10 separate MD realizations to provide better statistics. Structural disorder slightly shifts the first-shell peak toward longer In-O distances; in addition, the In-O distance distribution widens to include a small fraction of the In-O bonds with longer distances, between 2.3 Å and 2.6 Å (Figure 2.1a). This behavior is common to other semiconductors such as Si. More striking changes occur in the O-O and In-In distance distributions, with both the O-O peak at 2.8 Å and the In-In peak at 3.4 Å—as well as the longer range peaks—suppressed in the amorphous case. The disorder-induced changes in the O-O distribution set the ionic AOSs apart from the covalent silica-based glasses, where the O-O peak is preserved, signifying that the oxygen environment around the main-group metals (with well-defined O-O distances in the highly symmetric Si-O polyhedra) is maintained upon amorphization. Because the strength of the M-O bonding determines the rigidity of the local polyhedral structure, indium oxide, having the weakest bonding among the posttransition metal oxides considered in this work, features the largest average distortions in the first-shell M-O polyhedra (Table 2.1). Therefore, despite seemingly unchanged first-shell In-O distribution upon amorphization, the short-range (nearest-neighbor) disorder should be expected from the distortions associated with the loss of symmetry and significant bond deviations within individual In-O polyhedra. In the medium range, at $\sim 3.2 \text{ \AA}$ and above (Figure 2.1a), the broader In-In distance distribution suggests that sharing of the neighboring In-O polyhedra changes significantly upon amorphization, as indeed can be seen from the structural comparison given in Figure 2.1c and 2.1d. The changes in In-O polyhedra sharing will be quantified in Section 2.7.

To determine the optimal density of amorphous In₂O₃, at least 10 independent MD liquid-quench simulations were performed for five different density values. Upon equilibration of each configuration at 300 K for 6 ps, the DFT total energy was calculated as an average over the final (stable) 500 MD steps to remove thermal fluctuations.

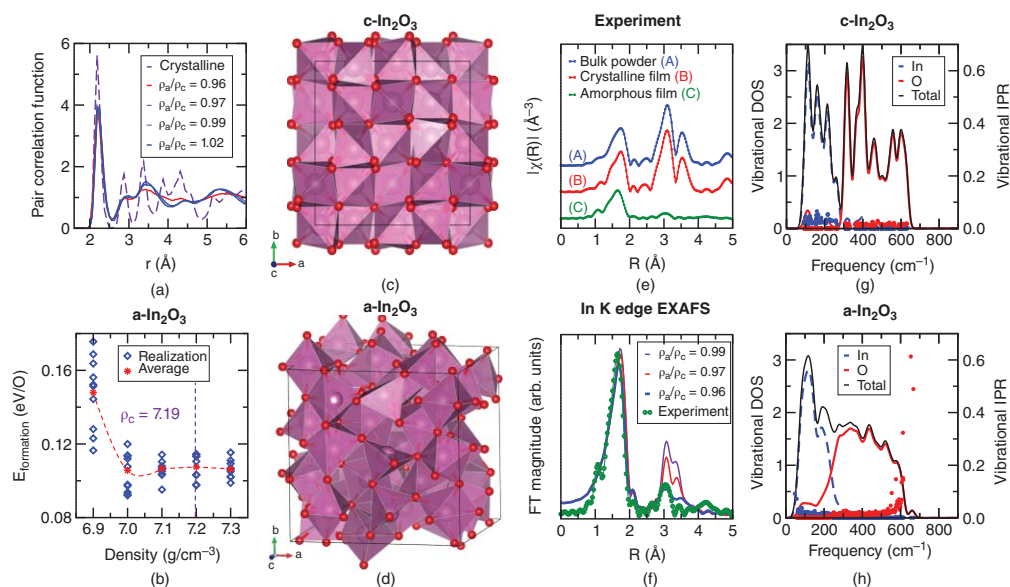


Figure 2.1 General structural properties of In_2O_3 . (a) Total pair-correlation function for crystalline (bixbyite) and amorphous In_2O_3 with different densities. Both crystalline (dashed line) and amorphous (solid lines) results were obtained from MD simulations at 300 K (equilibration with 3,000 MD steps = 6 ps). The results for amorphous structures represent an average over at least 10 separate MD realizations at each density. (b) The energy-density curve for amorphous In_2O_3 calculated as $E_{\text{formation}} = E_{\text{TOT}}(\text{amorphous}) - E_{\text{TOT}}(\text{crystalline})$. Upon equilibration of each configuration at 300 K for 6 ps, the DFT total energy was calculated as an average over the final (stable) 500 MD steps to remove thermal fluctuations in each of the 10 realizations (diamond); the average over the realizations is represented by a star symbol. (c,d) Crystalline and amorphous atomic structures with In-O polyhedra highlighted. In and O atoms are represented by large and small spheres, respectively. (e) Experimental extended X-ray absorption fine structure (EXAFS) for an In K edge in bulk powder, crystalline film, and amorphous film samples of In_2O_3 . (f) Calculated EXAFS for an In K edge in amorphous In_2O_3 models with different densities (solid line) as compared to experimental spectra for amorphous film (line with circle symbols). (g,h) Total and partial vibrational density of states (VDOS) and vibrational inverse participation ratio (VIPR) calculated for crystalline and the most stable amorphous In_2O_3 structures. In (O) states are represented by dashed (solid) thick lines, and the total VDOS is a thin solid line.

Table 2.1 First-shell effective coordination number (ECN), effective average distance, and distortion for metal and oxygen atoms for crystalline and amorphous binary oxides at different densities.

	Density, g/cm ³	Metal–Oxygen			Oxygen–Metal					
		ECN	$l_{av}, \text{Å}$	$\sigma^2, \times 10^4 \text{Å}^2$	ECN	$l_{av}, \text{Å}$	$\sigma^2, \times 10^4 \text{Å}^2$			
<i>c</i>-In₂O₃	7.20	5.84	2.17	33	3.84	2.17	50			
		5.73	2.17	57						
<i>a</i> -In ₂ O ₃	7.30	5.38	2.19	124	3.65	2.20	126			
	7.20	5.38	2.20	121	3.64	2.20	126			
	7.10	5.35	2.20	127	3.62	2.20	132			
	7.00*	5.32	2.21	132	3.60	2.21	135			
	6.90	5.14	2.18	141	3.50	2.19	136			
<i>c</i>-SnO₂	6.95	5.90	2.05	19	2.95	2.05	19			
		5.50	2.09	119						
<i>a</i> -SnO ₂	6.81	5.50	2.09	119	2.80	2.09	97			
	6.48*	5.41	2.09	117	2.76	2.09	98			
	6.17	5.26	2.09	116	2.70	2.09	91			
	5.88	5.14	2.09	118	2.72	2.10	91			
<i>c</i>-ZnO	5.61	3.91	1.98	25	3.91	1.98	24			
		3.80	2.00	104						
<i>a</i> -ZnO	5.78	3.80	2.00	104	3.80	2.00	106			
	5.50	3.70	2.00	99	3.70	2.00	96			
	5.23*	3.64	2.00	96	3.65	2.00	106			
	4.98	3.53	1.99	102	3.50	2.00	108			
<i>c</i>-Ga₂O₃	6.44	3.93	1.84	16	3.46	1.96	139			
		5.59	1.98	75				2.89	1.87	38
								2.83	1.90	55
<i>a</i> -Ga ₂ O ₃	6.12	4.67	1.93	123	3.19	1.94	115			
	5.80	4.50	1.92	115	3.10	1.94	110			
	5.50	4.34	1.92	97	2.94	1.92	96			
	5.23*	4.26	1.92	87	2.85	1.92	90			
	4.97	4.16	1.91	79	2.77	1.91	87			

Note: The values represent an average over all metal or oxygen atoms in the supercell and over 10 separate MD realizations at the given density. Bixbyite, rutile, wurtzite, and monoclinic β -phase structures are considered for crystalline In₂O₃, SnO₂, ZnO, and Ga₂O₃, respectively.

The results, shown in Figure 2.1b, suggest that (i) the formation energy of different MD realizations varies within at least 0.02 eV/atom, and the variation is largest for the lowest density case, most likely due to differences in morphology; (ii) several MD realizations (or bigger cells) are required to predict the optimal density; and (iii) there is a substantial overlap between the total energy for the configurations with different densities, giving an extremely shallow minimum in the energy–density plot. The latter signifies that amorphous indium oxide samples with density values within a wide range (7.00–7.30 g/cm³) could be grown. Different deposition techniques and pre- or postdeposition conditions are likely to affect the density of amorphous In₂O₃ oxide. Moreover, we speculate that the density of amorphous In₂O₃ may change long after the sample was deposited, making the structural characterization challenging. In the discussion here, amorphous indium oxide structures with a density of 7.00 g/cm³ are used; this optimal density is slightly lower than the crystalline density of 7.19 g/cm³.

To validate the theoretical amorphous models, the EXAFS is calculated for the In K edge for amorphous In_2O_3 models with different densities. From experimental EXAFS (Figure 2.1e), the peak that corresponds to the indium first shell (In-O) is maintained, whereas the second-shell (In-In) peak is significantly suppressed upon amorphization, in accordance with our pair-correlation function results (Figure 2.1a). Overall, an excellent agreement between the theoretical and experimental EXAFS is obtained (Figure 2.1f). Moreover, the results further corroborate the crucial effect that density has on the In-In distances and coordination (Figure 2.1f).

Next, total and partial VDOSs were calculated for crystalline and the most stable amorphous In_2O_3 structures to verify the dynamical stability of the latter structure and to identify disorder-induced changes. In addition, the VIPR was calculated from the normalized displacement vectors to determine the localization of different vibrational modes. The results, shown in Figure 2.1e and 2.1f, demonstrate that disorder not only makes the VDOS featureless by smearing and suppressing the well-defined peaks within the entire range of frequencies, but also leads to a notable overlap between the In and O VDOSs. The overlap occurs primarily due to a shift of the oxygen VDOS toward the lower frequencies. Similarly, the In VDOS develops low-frequency modes that do not exist in bixbyite In_2O_3 . The VDOS shifts toward lower frequencies for both oxygen and indium are characteristic of amorphous phases. At the same time, several oxygen atoms that oscillate at normal modes with high frequencies of around $550\text{--}650\text{ cm}^{-1}$ (with the largest VIPR value of 0.6) and several In atoms that oscillate with low frequencies of 50 cm^{-1} (the largest VIPR value of 0.1) appear in the amorphous phase, whereas the remaining frequencies show low VIPR values, comparable to those in the crystalline mode and suggesting an evenly distributed vibration among different atoms within most of the spectrum.

Our comprehensive structural analysis begins with a comparison of the ECN distributions for the first-shell In-O and O-In polyhedra for the crystalline and amorphous indium oxide with perfect stoichiometry (i.e., for the oxygen-defect-free structures; Figure 2.2a). To account for room-temperature atomic fluctuations, the ECN is calculated for each individual In and O atom as a time average obtained from MD simulations at 300 K for 3,000 steps (6 ps). For amorphous phases, we analyzed 10 independent MD realizations at the optimal density; Figure 2.2 combines the results for the 10 realizations.

In bixbyite In_2O_3 , there are two non-equivalent In sites, 8b and 24d; the former represents a perfect octahedron with six oxygen neighbors located at a distance of 2.17 \AA and an ECN of 6.00, whereas the latter is a distorted octahedra with two O neighbors at 2.13 \AA , two at 2.20 \AA , and two at 2.23 \AA , making the average In-O distance to be 2.18 \AA and $\text{ECN} = 5.91$ for the 24d site. At room temperature, the atomic vibrations reduce the ECN of the two In types to 5.84 and 5.73, respectively, and the effective average In-O distance is slightly reduced to 2.17 \AA for the 24d site (Table 2.1). Importantly, the temperature effects make the two types of In atoms indistinguishable, representing both with a single-peaked broad distribution of ECN (Figure 2.2a). Oxygen atoms in crystalline In_2O_3 are four-coordinated with In neighbors. At room temperature, the average effective coordination of oxygen atoms is 3.84.

ECN distributions for crystalline and amorphous In_2O_3 are shown in Figure 2.2a. Clearly, both indium and oxygen distributions become nearly two times wider upon amorphization. The number of “fully” coordinated In and O atoms is suppressed; moreover, secondary peaks at $\text{ECN}(\text{In}) = 5$ and $\text{ECN}(\text{O}) = 3$ become visible. Thus, despite the similarities in the nearest-neighbor indium–oxygen distance distributions in the crystalline and amorphous phases (Figure 2.1a), disorder leads to significant bond deviations in individual polyhedra, reducing the coordination numbers for a large fraction of In-O and O-In. The average ECN values for different densities are given in Table 2.1.

As can be expected, the angle distributions for both O-In-O and In-O-In also widen and become more uniform in the amorphous In_2O_3 (Figure 2.2b). As mentioned in Section 2.1, the distortions in the O-In polyhedra are expected to have a more pronounced effect on the electronic properties of AOSs due to the directional nature of the O-*p*-orbitals as compared to the symmetry-indifferent spherical In-*s*-orbitals [14]. It should be noted here that the In-O-In angle also can be viewed as a measure of the mutual alignment of neighboring InO polyhedra. In bixbyite In_2O_3 , the peak at about $\text{In-O-In} = 128^\circ$ corresponds to the corner-shared InO_6 polyhedra; this peak

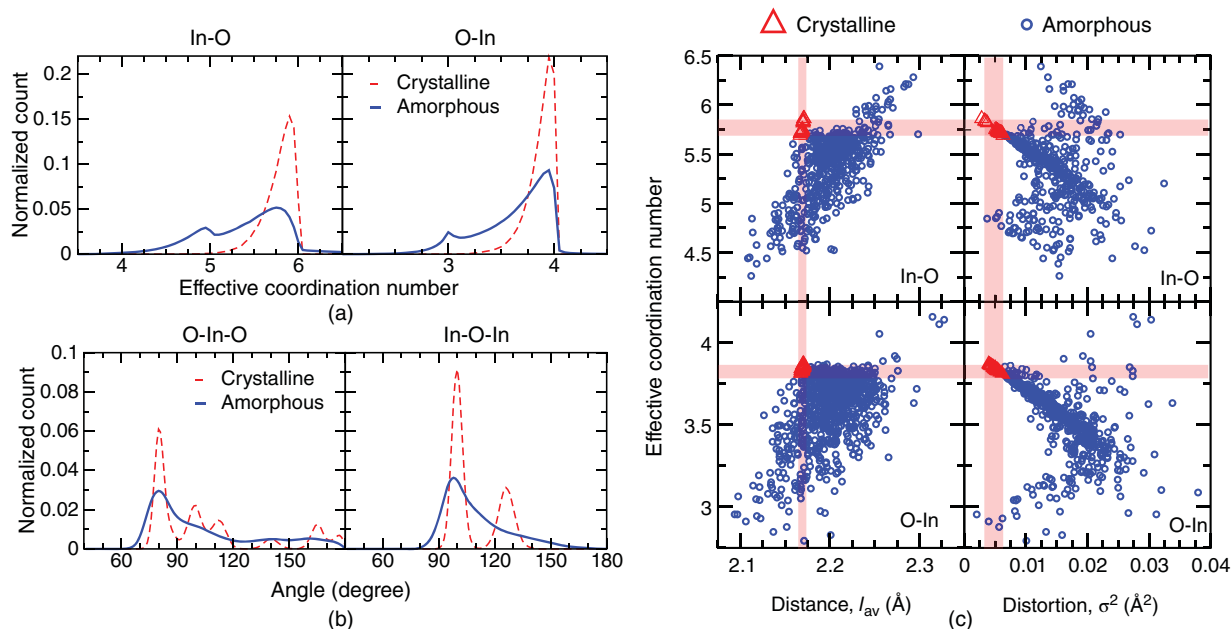


Figure 2.2 Structural randomness: The properties of individual In-O and O-In polyhedra in In_2O_3 . (a) Distribution of the effective coordination number of In and O in crystalline (dashed line) and amorphous (solid line) phases. (b) Distribution of the O-In-O and In-O-In angles in crystalline (dashed line) and amorphous (solid line) phases. The results for amorphous structures represent an average over at least 10 separate MD realizations at optimal density. (c) Effective coordination number of individual In and O as a function of the effective average distance or distortion for the given atom in crystalline (triangles and shaded region) and 10 amorphous (circles) phases. All results are calculated based on the MD simulations at 300 K (equilibration with 3,000 MD steps = 6 ps).

is strongly suppressed in the amorphous phase, suggesting a significant disorder in the medium-range structure even though the density of the amorphous structure is only 3% lower than that in the crystalline oxide.

The remarkable difference between crystalline and amorphous In_2O_3 can be best visualized when the time-averaged ECN values for the individual In and O atoms are plotted as a function of their time-averaged effective distance and distortion (Figure 2.2c). Strikingly, despite the similarity of the In-O distance distributions for crystalline and amorphous oxides (Figure 2.1a), only four In atoms out of 540 within the 10 MD realizations have structural values that are similar to those in bixbyite In_2O_3 (i.e., $5.70 < \text{ECN} < 6.00$ and $\sigma^2 < 0.0060$), although all four have the effective average In-O distance of 2.20 Å, which is above the corresponding average crystalline distance of 2.17 Å. Importantly, the amorphous oxide features a notable fraction of In atoms that are undercoordinated ($\text{ECN} < 5.0$) and have low distortions ($\sigma^2 < 0.01$ Å²) as well as those that are overcoordinated ($\text{ECN} > 6.0$) (Figure 2.2c). Similar observations can be done for oxygen atoms. For the majority of atoms, however, there are two clear correlations: (i) the lower the ECN value, the larger the distortions in the polyhedral are; and (ii) the reduction in ECN value is generally associated with shorter average bond length, as should be expected for an ionic material. While the spherical symmetry of the In *s*-states makes the In atoms indifferent to the exact direction in which the oxygen neighbors are located (the distribution of the O-In-O angles is wide and uniform; Figure 2.1b), the overlap between the spherical *s*-orbital of In and the *p*-orbitals of O atoms may be affected by changes in the In-O distances. This situation will be discussed in the electronic localization section of this chapter (Section 2.7).

Thus, disorder leads to significant bond deviations and reduced effective coordination numbers for individual In and O atoms, even though the density of amorphous oxide is lower by less than 3% as compared to that in the